Type I IFNs promote cancer cell stemness by triggering the epigenetic regulator KDM1B

Antonella Sistigu (antonella.sistigu@unicatt.it)
Università Cattolica del Sacro Cuore
Martina Musella
Università Cattolica del Sacro Cuore
Claudia Galassi
Università Cattolica del Sacro Cuore
Andrea Guarracino
University of Rome “Tor Vergata” https://orcid.org/0000-0001-9744-131X
Gwenola Manic
Italian Institute for Genomic Medicine, Candiolo Cancer Institute
Nicoletta Manduca
Università Cattolica del Sacro Cuore
Marco Pietrosanto
Università Tor Vergata
Manuela Helmer-Citterich
Università Tor Vergata
Matteo Pallocca
Regina Elena National Cancer Institute
Maurizio Fanciulli
Regina Elena National Cancer Institute
Anna Di Benedetto
Regina Elena National Cancer Institute
Cristiana Ercolani
Regina Elena National Cancer Institute
Edoardo Pescarmona
Regina Elena National Cancer Institute
Laura Pizzuti
Regina Elena National Cancer Institute
Francesca Sperati
Regina Elena National Cancer Institute
Michele Signore
Istituto Superiore di Sanità
Sara Vitale

Università Cattolica del Sacro Cuore
Giovanna Schiavoni
Istituto Superiore di Sanità
Fabrizio Mattei
Istituto Superiore di Sanità
Adele De Ninno
Italian National Research Council
Luca Businaro
Italian National Research Council
Valeria Lucarini
Bambino Gesù Children's Hospital
Laura Bracci
Istituto Superiore di Sanità
Eleonora Aricò
Istituto Superiore di Sanità
Giovanna Ziccheddu
Regina Elena National Cancer Institute
Francesco Facchiano
Istituto Superiore di Sanità
Stefania Rossi
Istituto Superiore di Sanità
Massimo Sanchez
Istituto Superiore di Sanità
Alessandra Boe
Istituto Superiore di Sanità
Mauro Biffoni
Istituto Superiore di Sanità
Ruggero De Maria (ruggero.demaria@unicatt.it)
Università Cattolica del Sacro Cuore
Ilio Vitale (ilio.vitale@iigm.it)
Italian Institute for Genomic Medicine, Candiolo Cancer Institute

---

Article

Keywords: viral mimicry, immunogenic cell death, epigenetic editing, demethylation, tumor-initiating cell death, immunotherapy

Posted Date: May 5th, 2021

DOI: https://doi.org/10.21203/rs.3.rs-436936/v1

Version of Record: A version of this preprint was published at Nature Immunology on August 24th, 2022.
See the published version at https://doi.org/10.1038/s41590-022-01290-3.

Abstract

Cancer stem cells (CSCs) are immature, immortal cells within tumors, adept at resisting therapeutic pressure and responsible for local and distant disease recurrence. Non-genetic mechanisms of acquired resistance are increasingly being described, however molecular insights into this evolutionary process still lack. Here, we showed that Type I interferons (IFNs-I) act as molecular hubs of resistance during immunogenic chemotherapy, as they trigger the epigenetic regulator KDM1B, responsible for an adaptive, yet reversible, transcriptional rewiring of cancer cells towards stemness and immune escape. Accordingly, KDM1B pharmacological inhibition antagonizes the appearance of IFN-I-adapted CSCs, both in vitro and in vivo. Notably, IFN-I-adapted CSCs are heterogeneous in terms of multidrug resistance, plasticity, invasiveness and immunogenicity. Moreover, in breast cancer patients receiving anthracycline-based chemotherapy, IFN-I and KDM1B signatures positively correlate with CSC and immune evasion markers. Our study identifies IFN-I→KDM1B axis as a potent engine of cancer cell reprogramming and recommends KDM1B targeting an attractive adjunctive to immunogenic drugs to prevent CSC expansion and increase the long-term benefit of therapy.

Introduction

Despite the significant progress made over the last decades, the cure of cancer still remains one of the greatest medical challenges. Indeed, even neoplasms initially responding to conventional, targeted or immune-based therapies could acquire resistance and/or relapse into more aggressive and metastatic malignancies[1, 2]. Therapy resistance occurs through a multifactorial, evolutionary process involving the acquisition of specific genetic and/or epigenetic alterations, which endow rare cancer cell variants with increased adaptiveness or fitness[3]. Like all evolutionary processes, cancer evolution is governed by the environment, and in particular by the changes inflicted by antitumoral treatments, which ultimately unleash tumor plasticity and generate evasive cell clones[4, 5, 6, 7].

Cancer stem cells (CSCs), also known as tumor-initiating or tumor-promoting cells, are the stem-like cell subpopulation within the tumor capable of self-renewal, multi-lineage differentiation, and responsible for tumor initiation, progression, metastatic spreading and therapy resistance[8, 9]. Historically considered rare and quiescent, CSCs, in specific cancer types, have progressively been demonstrated to be relatively abundant, highly proliferating, and able to evolve over space and time leading to a high degree of genotypic, phenotypic and functional heterogeneity[9, 10]. Moreover, non-CSC subsets can adapt to the changes of the tumor microenvironment (TME) by undergoing cell reprogramming and (re)generating CSCs[9].

Epigenetic dysregulations critically affect cancer-immune cell interactions and co-evolution during disease onset, progression and response to therapy by influencing cellular states and fates[11]. Not surprisingly given their role in normal stem cell maintenance, epigenetic mechanisms have also been involved in the preservation of CSCs[12]. This feature, together with the inherent reversibility of epigenetic

modifications, makes the use of epigenome-targeting drugs (epidrugs) a unique opportunity to rationally target CSCs in combination with conventional therapies[11, 13, 14, 15, 16].

One key concept in tumor immunology is that some chemotherapeutics, including (but not limited to) anthracyclines (*e.g.*, doxorubicin, DOX), oxaliplatin (OXP) and cyclophosphamide[17, 18] induce cancer immunogenic cell death (ICD), a form of regulated cell death that initiates adaptive immune responses by the emission of damage-associated molecular patterns (DAMPs)[19, 20]. These include Type I interferons (IFNs-I), a family of cytokines that act as chemoattractants for T cells by triggering the production of the IFN-stimulated gene (ISG) C-X-C motif chemokine ligand 10 (CXCL10) upon binding to interferon alpha and beta receptor (IFNAR)[18]. Nonetheless, depending on the duration and intensity of the transduced signaling and/or the nature of the unleashed ISGs, IFNs-I can also display pro-tumorigenic effects[21], promoting the expression of the immune checkpoint (IC) ligand CD274 (best known as PD-L1)[18, 22, 23] and fostering cancer immunoediting[24]. Moreover, innate immune signaling upstream of IFNs-I has been associated with nuclear reprogramming and malignant transformation[25].

In this work, we elucidated the downside of IFNs-I during ICD. Specifically, we showed that IFNs-I reprogram cancer cells toward a more aggressive, stem-like phenotype by recruiting the demethylase 1B (KDM1B), an epigenetic regulator also known as LSD2, which erases mono- and di-methyls on histone H3 at lysine 9 (H3K4me1 and H3K4me2)[26]. Such detrimental resetting represents a hitherto undescribed mechanism of tumor evolution, which drives acquired resistance and immune evasion. We term this process “regress to progress”. Dissecting IFN-I dichotomy in cancer immune surveillance and escape offers key insights that could help develop rationale-based combinational strategies and increase the chances of success in cancer medicine.

Results

Exogenous IFN-I administration promotes the enrichment and *de novo* induction of putative CSCs.

To investigate the impact of the IFN-I→IFNAR axis on the appearance of cancer cells with a stem-like phenotype (hereafter referred to as CSCs), we selected a panel of cancer cell lines of distinct origin (epithelial or mesenchymal) and species (human or mouse) and treated them for 72h with IFNs-I before assessing, by flow cytometry, the levels of prominin 1 (Prom1, best known as CD133), CD24 and CD44 surface markers, whose expression, alone and in combination, has been associated with putative CSCs. We observed that IFN-I exposure favors the enrichment of rare, $CD133^{+}CD24^{+}CD44^{+}$ putative CSCs in all analyzed murine cancer cell lines. Specifically, we identified two main populations of IFN-I-enriched CSCs (IFN-CSCs) in MCA205 sarcoma cells: the $CD133^{+}CD24^{+}CD44^{+low}$ (CD44L) and the $CD133^{+}CD24^{+}CD44^{+high}$ (CD44H) CSC subsets (**Figure 1a**). Putative IFN-CSC fractions were also detected in AT3 breast carcinoma (BC), namely the $CD133^{+}CD44^{+}CD24^{+low}$ (CD24L) and $CD133^{+}CD44^{+}CD24^{+high}$ (CD24H) CSC subsets, whereby we focused exclusively on the former, the widely recognized CSC subpopulation in BC[27] (**Figure 1a**). Similarly, we found (*i*) $CD133^{+}CD44^{+}CD24^{+}$ in CT26 colon carcinoma

cell line and (*ii*) $CD133^+CD44^+CD24^{+low}$ and $CD133^+CD44^+CD24^{+high}$ in B16.F10 melanoma cell line (**Supplementay Figure 1a**). These results are in line with the intra- and inter-tumoral heterogeneity often ascribed to CSCs[28]. To assess whether this phenomenon was exclusive of the murine cancer model, we treated human U2OS osteosarcoma and MDA-MB-231 BC cell lines with recombinant human IFN-α2a and then analyzed the expression of standard human CSC markers. As expected, we detected IFN-CSC subpopulations in both U2OS ($CD133^+CD44^+$ and $CD44v6^+CD24^+$ cell subsets) and MDA-MB-231 ($CD133^+CD44^+$ and $CD44v6^+CD24^{+low}$ cell subsets) cell lines (**Supplementary Figure 1b**).

We then investigated whether IFN-CSC enrichment relied on the positive selection of pre-existing CSCs or on an active *de novo* induction of CSCs, a strategy cancer cells might deploy to evolve resistance. To address this question, we isolated MCA205 $CD133^+$ and $CD133^-$ (*i.e.*, non-CSC) cell fractions by fluorescence-activated cell sorting (FACS) and treated them with IFNs-I. Intriguingly, by flow cytometry, we found that IFN-I treatment led to a significant increase in the fraction of CD44H cells and the levels of the pluripotency transcription factor (TF) SRY (sex determining region Y)-box 2 (SOX2) in both the $CD133^+$ and $CD133^-$ subsets (**Figure 1b**). In parallel quantitative RT-PCR (qRT-PCR) analyses of common stem-related TFs and CSC markers, we found that exogenous IFNs-I significantly upregulate Kruppel-like factor 4 (*Klf4*), POU domain, class 5, transcription factor 1 (*Pou5f1*, best known as *Oct3/4*), *Sox2* and nestin (*Nes*) in FACS-isolated $CD133^-$ cells and Nanog homeobox (*Nanog*) in FACS-isolated $CD133^-$ and $CD133^+$ cells (**Figure 1b**). These results suggest the co-occurrence of a process of positive selection of rare, pre-existing CSCs along with *de novo* CSC induction in response to exogenous IFNs-I.

We further analyzed the phenotypic and transcriptional profiles of IFN-CSCs, observing that IFN-I-treated epithelial cancer cells (AT3 and B16.F10) acquired a typical stem-like elongated morphology (**Supplementary Figure 1c**). Moreover, in distinct murine cancer cells, IFNs-I promoted the emergence of the side population (SP, a *bona fide* CSC feature), which was significantly reduced by co-treatment with verapamil (VRP), a blocker of ATP-binding cassette (ABC) transporters (**Figure 1c** and **Supplementary Figure 1d**). Finally, IFN-I exposure induced significant upregulation of *Klf4*, *Oct3/4*, *Sox2*, *Nanog*, hes family bHLH transcription factor 1 (*Hes1*) and *Nes* (**Figure 1d** and **Supplementary Figure 1e**), and endowed MCA205 and AT3 cancer cells with increased sphere forming ability (**Figure 1e**). Notably, only spheres pre-exposed to IFNs-I retained a CSC-related phenotypical and transcriptional profile when serially plated in standard CSC culture conditions (**Figure 1f**).

These data collectively demonstrate that exogenous IFNs-I favor the appearance of putative CSCs in multiple murine and human cancer cell lines.

IFN-I signaling, during immunogenic chemotherapy, triggers cancer cell stemness.

Since we have previously shown a key role for IFNs-I during *bona fide* ICD[18], we asked whether CSC subpopulations could also be enriched during immunogenic chemotherapy. We took advantage of a library of pre-validated MCA-derived clones deficient for cardinal elements of the IFN-I pathway, including: (1) *Ifnar1*, (2) stimulator of interferon response cGAMP interactor 1 (*Sting1*, best known as *Sting*), (3) toll-

like receptor 3 (*Tlr3*), (4) toll-like receptor adaptor molecule 1 (*Ticam1*, best known as *Trif*), (5) interferon induced with helicase C domain 1 (*Ifih1*, best known as *Mda5*), and (6) mitochondrial antiviral-signaling protein (*Mavs*, also known as *Ips-1*) (**Figure 2a**)[18]. We exposed these clones to the ICD inducer OXP ("donor" dying cells), then co-cultured "donor" dying cells with untreated clones of the same genotype ("receiving" viable cells) for 24h, and finally analyzed "receiving" cells at phenotypic and transcriptional levels (**Supplementary Figure 2a**). Similar to what observed upon IFN-I treatment, wild-type (*Wt*) clones responding to OXP displayed a significant increase of the two CD44H and CD44L CSC subpopulations (**Figure 2b**), which we will refer to as "ICD-CSCs". Notably, ICD-CSC enrichment was impaired only in *Ifnar*$^{-/-}$ clones, indicating dependence on IFN-I signaling (**Figure 2b**). Consistently, both IFN-I and OXP treatment induced the accumulation of CSC-related transcripts in *Wt* clones and (even if to a lesser and heterogeneous extent) in *Sting1*$^{-/-}$, *Tlr3*$^{-/-}$, *Ticam1*$^{-/-}$, *Ifih1*$^{-/-}$ and *Mavs*$^{-/-}$ clones, yet failing in *Ifnar*$^{-/-}$ clones (**Figure 2c**). Similarly, the ICD inducer DOX favored a complete transcriptional rewiring toward pluripotency by enhancing the expression of the entire panel of reprogramming factors analyzed, while the non-ICD drug cisplatin (CDDP), which we previously shown to induce very low levels of IFNs[18], affected the expression of only few transcriptional factors (**Figure 2d**). OXP also promoted the appearance of a SP in all murine cancer cell lines (**Figure 2e** and **Supplementary Figure 2b**). Moreover, by exploiting DOX red fluorescence, we observed two distinct cell subsets (DOX^{+low} and DOX^{+high}) in DOX-treated MCA205 cells, differing in their capability to extrude DOX as well as Hoechst 33342 (**Figure 2f** and **Supplementary Figure 2c**). Notably, following drug withdrawal, only DOX^{+low} cells survived and resisted re-challenge with diverse ICD inducers (**Supplementary Figure 2d**), indicating their multidrug tolerance/resistance[29]. To explore the *in vivo* appearance of ICD-CSCs, we locally treated MCA205 tumors growing in syngeneic immunocompetent mice with DOX or CDDP and evaluated CSC enrichment in recollected xenografts 15 days post-treatment (*i.e.*, when tumors start escaping growth control[18]). Strikingly, we found a twofold increase of CD44H and NANOG^{+}, upon DOX but not CDDP administration (**Figure 2g**).

Altogether, these results demonstrate that IFNs-I, during immunogenic chemotherapy, promotes CSC enrichment, both *in vitro* and *in vivo*, and point to this effect as an adaptive response cancer cells may deploy to escape therapy control.

Horizontal transfer of nucleic acids from dying to viable cancer cells, upstream of IFN-I signaling, drives cancer stemness.

To dissect the molecular mechanisms underlying ICD-CSC enrichment, we co-cultured OXP-treated "donor" MCA205 cells with untreated "receiving" MCA205 cells alone or in combination with benzonase (BNZase), which degrades all nucleic acids, or RNase A, RNase H or DNase, which selectively degrade ssRNAs, dsRNAs or DNA. We observed differential effects in the two CD44H and CD44L ICD-CSC subsets, with BNZase preventing the enrichment of both CSC populations, while RNase A, RNase H and DNase significantly affecting only CD44L cells (**Figure 3a**). Accordingly, BNZase halved the proportion of ICD-CSCs in "receiving" AT3 and CT26 cells (**Supplementary Figure 3a**). The observation that only the

depletion of all nucleic acids nullifies the enrichment of ICD-CSCs, again suggests that this phenomenon depends on an intact IFN-I signaling.

We next investigated the involvement of extracellular vesicles (EVs) in ICD-CSC enrichment. EVs isolated from “donor” MCA205 cells and stained with the non-toxic fluorescent membrane dye PKH26 were added to “receiving” MCA205 cells (**Supplementary Figure 3b**). EV uptake in “receiving” cells, confirmed by fluorescence microscopy and flow cytometry (**Figure 3b**), induced a significant increase of CD44H and CD44L CSC percentages and of the expression of most reprogramming factors, which were prevented by co-treatment with the actin inhibitor cytochalasin D (cyto D) (**Figure 3c,d**). Intriguingly, EVs from OXP-treated cancer cells carried mRNAs for reprogramming factors (*Klf4*, *Myc*, *Oct3/4*, *Sox2*, *Nanog*, *Hes1*, *Nes*), invasion molecules [snail family zinc finger 1 (*Sna1*, best known as *Snail*), Twist-related protein 1 (*Twist1*, also known as *bHLHa38*), Cadherin-2 (*Cdh2*, also known as *N-cadherin/Ncad*), Vimentin (*Vim*), and Fibronectin (*Fn1*)] and ICs, [*Pdl1*, programmed cell death 1 ligand 2 (*Pdcd1lg2*, also known as *Pdl2*), and lectin, galactose binding, soluble 9 (*Lgals9*, best known as *galectin-9*) **Figure 3e**], suggesting their contribution to cancer cell de-differentiation and aggressiveness during immunogenic chemotherapy.

Altogether, these data indicate that ICD-CSC enrichment occurs through paracrine processes involving free and EV-mediated transfer of nucleic acids and stem-related mRNAs.

IFN-CSCs and ICD-CSCs exhibit heterogeneity of drug-response, tumorigenic and invasive potential, and immunogenicity.

We then analysed FACS-isolated CD44H and CD44L ICD-CSCs separately, and searched for hallmark CSC features like chemo-refractoriness, self-renewal ability, tumorigenic and metastatic potential, and the capability to escape immune control. We treated CD44H and CD44L cells with various ICD inducers, and found a diverse sensitivity to drugs, with only CD44H cells showing a higher therapeutic resistance than parental counterparts, both *in vitro* (**Supplementary Figure 4a**) and *in vivo* (**Figure 4a**), upon transplantation in immunocompetent mice. On the one hand, by monitoring the *in vitro* evolution of FACS-isolated MCA205 ICD-CSCs, we demonstrated as both subsets were able to rapidly regenerate the phenotypic complexity of parental cells (**Figure 4b**). On the other hand, *in vivo* studies revealed that CD44H ICD-CSCs are significantly more tumorigenic and less immunogenic than CD44L ICD-CSCs. Indeed, although both subpopulations were able to generate tumors in immunocompromised NOD SCID gamma (NSG) mice, only CD44H ICD-CSCs developed neoplasms at the lowest doses and overcame immunosurveillance thus growing in immunocompetent hosts at the highest number of injected cells (**Figure 4c**). Consistently, only half of the immunocompetent mice rejecting CD44H ICD-CSCs were vaccinated against viable parental cells (**Figure 4d**). Conversely, CD44L ICD-CSCs or parental MCA205 cells endowed animals with 100% long-term protection against tumor re-challenge. Moreover, when intravenously injected into immunocompetent mice, CD44H (but not CD44L) ICD-CSCs developed lung metastases (**Figure 4e**).

Since we identified CD44H ICD-CSCs as the MCA205 subpopulation mainly driving *in vivo* tumor aggressiveness and therapeutic resistance, we focused on this subset. To gain insights into the

immunogenicity of ICD-CSCs, we analyzed the proliferation rate of isolated $CD8^+$ H-2Kb/ovalbumin (OVA)-specific OT-1 T cells previously primed with dendritic cells (DCs) that had taken up apoptotic OVA-expressing CD44H (CD44H-OVA) ICD-CSCs or parental cells, and then boosted with viable cells of the same type. In line with the immune privileged nature observed *in vivo* (**Figure 4c,d**), CD44H-OVA ICD-CSCs induced a significantly lower expansion of OT-1 CD8 T cells than parental conterparts (**Figure 5a**) and resisted CD8-mediated killing (**Figure 5b**). These data prompted us to hypothesize that CD44H ICD-CSCs could escape immune control by inducing CD8 T cell exhaustion. To pursue this hypothesis, we analyzed the expression of common IC ligands, finding the upregulation of PDL1, PDCD1LG2, CEA1 and LGALS9 (**Figure 5c**). Consistently, $CD8^+$ T tumor-infiltrating lymphocytes (TILs) isolated from MCA205-bearing mice 15 days after intratumoral injection of DOX (when CSC enrichment occurs), but not of CDDP (which does not enrich for CSCs), displayed a significant upregulation of the LGALS9 receptor IC Hepatitis A virus cellular receptor 2 (HAVCR2, best known as TIM-3) (**Figure 5d**). We extended the characterization of ICD-CSCs to AT3 cells (*i.e.*, the CD24L cell subset), and confirmed their regenerative potential (**Supplementary Figure 4b**) as well as the downregulation of the histocompatibility 2, K1 (H2-K1), and the upregulation of the IC ligands PDL1, PDCD1LG2 and LGALS9 (**Figure 5c**) and of the invasiveness markers *Snail*, *Twist1*, *Ncad* and *Fn1* (**Supplementary Figure 4c**).

To further characterize ICD-CSC immunogenicity, we measured cytokine production through Luminex Multiplex Assay, observing a unique chemokine secretion pattern in CD44H MCA205 and CD24L AT3 ICD-CSCs as compared to their respective parental cells. This encompasses reduced levels of proinflammatory chemokines CCL2 and CCL5, which mediate inflammatory monocyte trafficking and DC-T cell interactions[30], and enhanced capability to secrete CXCL1 and CXCL2 (the latter in CD24L AT3 cells), which promote chemoresistance and metastasis[31] (**Figure 5e**). Notably, CD24L AT3 cells also showed higher levels of the regulatory T cell chemoattractant CCL22[32] than parental AT3 cells. Accordingly, when CD24L ICD-CSCs or parental AT3 cells were confronted with histocompatible splenocytes in *ad hoc* microfluidic devices[33] and then analyzed by videomicroscopy for their *in vitro* capability to recruit immune cells, only parental cells were able to attract and stably interact with splenocytes at as early as 24h (**Figure 5f,g** and **Supplementary Movies 1-4**). On the contrary, CD24L ICD-CSCs failed to do so and, instead, migrated towards splenocytes starting a fleeting and unproductive interaction only upon 48h. Finally, when we confronted parental and CD24L AT3 cells in a microfluidic "competition" device (**Supplementary Figure 4d**), immune cells selectively migrated towards parental cells, moving away from CSCs (**Figure 5h,i**).

Altogether, these results allowed us to make several key observations: adaptation of cancer cells to immunogenic chemotherapy enables cell selection and drives phenotype switching. Both phenomena actively contribute to intratumor heterogeneity as the collection of CSC subpopulations have differential therapeutic response, aggressiveness and immunogenicity.

Global chromatin remodeling downstream of IFNs-I.

To dissect the mechanisms underlying cancer cell reprogramming downstream of IFNs-I, we mapped the chromatin landscape of parental (P) and CD44H (H) MCA205 cells by the assay for transposase-accessible chromatin using sequencing (ATAC-seq) (**Figure 6a-c**). By analyzing ATAC-seq peaks, we conceived a closed-to-open (C→O) and an open-to-closed (O→C) logic, and stratified genes in 4 groups. The C^PC^H and O^PO^H groups comprise genes with peaks permanently closed (*i.e.*, putatively repressed) or open (*i.e.*, putatively expressed) in both samples, while the C^PO^H and O^PC^H groups comprise genes whose peaks are closed in parental cells and open in CD44H IFN-CSCs and *viceversa*. In particular, we focused on the C^PO^H group containing genes putatively more expressed in CSCs. Intriguingly, this group encompasses genes involved in cancer stemness (*Myc* and *Sox*), embryonic development (*Tbx4*), epithelial-to-mesenchymal transition (EMT) (*Gata6* and *Tfcp2*), cancer cell invasiveness and metastatization (*Myct1*, *Spire1* and *Trpm4*), tumorigenesis, tumor progression and therapy resistance (*Slc6a6*, *Baiap2*, *Ttll7* and *Wee1*), the negative regulator of the antigen presentation machinery (APM) *Gpr17*, and the inhibitor of granzyme activity *Serpin* (**Figure 6a**). Consistently, in the O^PC^H group we found tumor suppressor genes (*Cdh*, *Cdk2ap1*, *Dlg2*, *Ripk3* and *Fbxw2*) and genes controlling tumor growth (*Mtor* and *Ncam1*), APM functionality (*Tap1*, *Tap2* and *Ctsl*) and inflammation (*Il24*, *Il27*, *Gsdmd* and *Uba7*) (**Figure 6a**). Subsequent integration with RNA-seq analyses confirmed an increased expression of genes involved in tumorigenesis, tumor progression, invasiveness (*e.g.*, *Csf1r*, *Trpm4*, *Itga5*, *Wee1*, *Baiap2*, *Ttll7* and *Spire1*) and immune escape (*e.g.*, *Gpr17*), coupled with repression of genes involved in tumor suppression and immune recognition (like *Cdh1*, *Il12b*, *Tlr5*, *Cdk2ap1*, *Il34*, *Il16* and *Ctsl*) in CD44H IFN-CSCs, as compared to parental cells (**Figure 6d**).

We next inferred and reconstructed protein–protein interaction subnetworks and biological processes specifically modulated in CD44H IFN-CSCs by using the clusterProfiler and enrichPlot R packages (**Figure 6e** and **Supplementary Figure 5a**). Gene ontology (GO) analysis showed that most of the upregulated genes in CD44H cells (red module) have significant functional connections with cell growth promotion, stemness maintenance and tissue remodeling, with immune suppression (*e.g.*, negative regulation of leukocyte activation), despite an intact response to IFN-I and IFN-II, with response to stress (*e.g.*, positive regulation of response to DNA damage stimulus, regulation of autophagy and apoptosis), lipid metabolism, and, of note, with enhanced chromatin accessibility. Accordingly, we organized the downregulated genes (blue module) into 4 biological processes: cell growth arrest, cell differentiation, oxidative phosphorylation and protein dephosphorylation. These results provide clues about the modular re-organization of specific pathways downstream of IFNs-I.

Of note, among the genes specific of the CSC fraction (CD44H cells), we also identified multiple ISGs, including (but not limited to) *Ifi27l2a*, *Ifi27l2b* and the epigenetic regulator *Kdm1b* (**Figure 6a,b**). We were particularly intrigued by *Kdm1b* since chromatin remodeling plays a critical role in cancer evolution, cellular plasticity and immune escape[12, 34, 35, 36]. At first, we measured the enrichment of TF-binding motifs in the ATAC-seq study by using the HOMER motif software (**Figure 6c** and **Supplementary Figure 5b**). We observed significant differences between CSCs and parental cells, in particular we found enrichment of motifs for various TFs of the helix-turn-helix (HTH) superfamily (*i.e.*, RFX, Rfx1, Rfx2, Rfx5

and X-box), the Homeobox basic helix-loop-helix (bHLH) member Pitx1:Ebox, the Rel homology domain (RHD) family member NFkB-p65, and the zinc finger (Zf) family member ZBTB in CD44H cells, suggesting their major role in the global chromatin remodeling in CSCs. Conversely, the Zf motifs CTCF, BORIS and NRSF, the transcriptional enhanced associate domain (TEA, TEAD) motifs (*i.e.*, TEAD and TEAD1-4), the Rel homology domain (RHD)-basic leucine-zipper (bZIP) superfamily member NFAT-AP1, the ETS, RUNT, the interferon-sensitive response element (ISRE) and the CCAAT box-binding transcription factor (CTF) motifs were more accessible in parental cells. Thereafter, we explored the role of the ISG KDM1B in the induction of ICD-CSCs. To this aim, we added the KDM1B inhibitor tranylcypromine (TCP) to the "donor"-"receiving" *in vitro* co-culture and found a significant reduction of CD44H percentages in "receiving" cells (**Figure 6f**). Of note, *in vivo* administration of TCP in MCA205 tumor bearing mice (**Figure 6g**, **left panel**), prevented the enrichment of ICD-CSCs as well as the induced expression of TIM-3 on $CD8^+$ TILs (**Figure 6g**, **central** and **right panels**).

Overall, these data demonstrate that KDM1B, downstream of IFNs-I, edits the epigenome of cancer cells toward stemness, immune escape and therapy resistance (**Figure 6h**).

IFN-I metagenes correlate with stemness in BC patients.

To investigate the clinical relevance of the IFN-I→KDM1B axis, we first calculated the Spearman correlation between *KDM1B*, IFN-I-related metagenes, stem-related reprogramming factors and IC ligands in multiple publicly available transcriptomic data of BC patients responsive to anthracyclines[18, 37]. We observed that the expression levels of *KDM1B* significantly correlated with those of *MYC* and *POU5F1* in two out of three available datasets and of *IFNB1*, *CXCL10*, and *CD274/PD-L1* in at least one dataset (**Figure 7a**). Along similar lines, *IFNB1* expression positively correlated with the expression of *SOX2* in half of the analyzed datasets, of *KLF4*, *NES* and *PDCD1LG2/PD-L2* in one dataset, and of *POU5F1* and *NANOG* in two datasets (**Figure 7a** and **Supplementary Figure 6a**). Similarly, the ISGs *MX1*, *CXCL10, DHX58, OASL* and *STAT1* correlated with the stemness factors *MYC*, *POU5F1*, *SOX2* and *NANOG*, and with the IC ligands *PDCD1LG2/PD-L2* and *CD274/PD-L1*, these last in turn correlating with *KLF4*, *MYC*, *POU5F1*, *SOX2* and *NANOG*, in at least one dataset (**Figure 7a** and **Supplementary Figure 6a**). Next, we selected a BC cohort including 1902 patients on the online biomarker validation tool Metabric (**Figure 7b,c** and **Supplementary Figure 6b-e**) and performed multivariate survival analysis by stratifying patients into two groups, according to risk behavior. In details, patients were assigned to either the high-risk or the low-risk group based on the high and low expression, respectively, of gene pairs selected among KDM1B-related, IFN-I-related and stem-related factors (*KDM1B-SOX2*, *MX1-SOX2*, *CXCL10-SOX2*, and *OASL-SOX2*). Of note, high-risk group patients exhibited a significantly reduced distant and local recurrence-free incidences (**Figure 7b** and **Supplementary Figure 6b-d**) and, accordingly, disease-specific survival was decreased if compared to low-risk group patients (**Figure 7c** and **Supplementary Figure 6e**).

To further correlate IFN-I and CSC signatures, we performed longitudinal immunohistochemistry (IHC) analyses on consecutive formalin fixed paraffin-embedded BC biopsies, assessing the expression of MX1 and CD44-CD24 on $CD45^-$ cancer cells at pre- (T0; at diagnosis) and post- (T1, at surgery) neo-adjuvant

anthracycline-based chemotherapy (**Figure 7d-f** and **Supplementary Table 1**). We found a significant increase of $CD44^{+}CD24^{-/+low}$ AIIred scores in 15% of cases (**Figure 7f**). Altogether, these results suggest the co-occurrence of IFN-I signature and CSC markers during anthracycline-based immunogenic chemotherapy.

Discussion

IFNs-I may either restrain or promote tumor growth depending on the duration and intensity of the transduced signaling, two features that jointly delineate the patterns of ISG expression, so-called "IFN signature"[21], and shape the accessibility to chromatin, so-called "IFN-mediated epigenomic signature"[38, 39]. The leverage of transcriptional and epigenetic changes defines cell responses to environmental hints and dictates the efficacy of natural and therapy-induced immunosurveillance[11, 17, 40, 41]. Here, we provide preclinical and clinical evidence that the acute induction of IFNs-I, as during chemotherapy-induced ICD, favors the appearance of subpopulations of CSCs. This occurs via positive selection of CSCs coupled to a KDM1B-dependent *de novo* reprogramming of cancer cells toward a stem-like phenotype. Therefore, beyond stimulating antitumor immune response, IFNs-I can foster malignant progression leaving a detrimental "imprint" on cancer cells.

Our study sheds light on the debated and poorly investigated contribution of IFN-I signaling on tumor heterogeneity and CSC induction. On the one hand, we and others previously reported that IFNs-I hinder CSC generation/survival, showing that the abrogation of steady-state endogenous IFN-I signaling leads to the emergence of breast CSCs in HER2/neu transgenic mice and triple-negative BC[42, 43]. On the other hand, acute production or exogenous administration of IFNs-I favored cancer stemness in mouse models of pancreatic cancer[44] and human BC and squamous carcinoma cell lines[45]. Nonetheless, in these studies the molecular mechanisms underlying IFN-I-CSC expansion have not been analyzed, and this phenomenon has been neither investigated in the context of ICD, nor associated with potential cancer cell reprogramming. In this respect, it appears of interest the evidence that the induction of the ISG *IFI27* in ovarian carcinoma biopsies and cell lines drives EMT, cancer stemness, invasiveness and therapeutic resistance[46]. Whether IFI27 is involved in ICD-CSC expansion requires further investigations. Based on our results, we surmise that, when produced at chronic low levels, IFNs-I limit CSC proliferation and survival, restraining tumor growth. At odds, acute IFN-I production, as during immunogenic chemotherapy, favors the survival of pre-existing CSCs and cancer cell de-differentiation, potentially leading to therapy resistance/failure.

Here, we also found a certain degree of phenotypic and functional heterogeneity within IFN-CSCs, consistently with the current view of an adaptable, evolutive and dynamic nature of CSCs[47, 48]. Moreover, we showed that specific IFN-I-CSC subsets are characterized by high resistance to (immuno)chemotherapy and *in vivo* tumorigenicity, metastatic potential and low immunogenicity, in line with previous observations[49, 50]. In our setting, CSC immunoprivilege encompasses a reduced capability of these cells to attract and stably interact with effector immune cells, in part due to decreased secretion

of proinflammatory chemokines and enhanced capability to suppress T cell activation, and in part due to upregulated expression of IC ligands and cognate receptors. At the mechanistic level, IFN-I-related immune escape has been previously associated with the upregulation in cancer (stem) cell of (*i*) PD-L1 and LGALS9[23], (*ii*) nitric oxide synthase 2 (NOS2), which favors the recruitment of regulatory cells[51], and (*iii*) Serpinb9, which inhibits granzyme B activity and thus $CD8^+$ T cell cytotoxicity[52]. Intriguingly, by integrating ATAC-seq and RNA-seq data, we found upregulation, in CD44H IFN-CSCs, of serpins and downregulation of *Uba7*, a tumor suppressor ISG which codes for a protein able to attract effector T cells[53]. Whether these factors play a major role in protecting CSC from immune attack remains to be established.

By co-culturing experiments, we demonstrated that ICD-CSC enrichment involves an autocrine/paracrine cancer cell-to-cancer cell circuitry centered on the IFN-I→IFNAR→KDM1B signaling pathway. We propose a model whereby CSC induction lies on the horizontal transfer of nucleic acids and possibly stem-related encoding mRNAs from cancer cells undergoing ICD to viable cancer cells. Notably, such intercellular communication can also occur via EVs, according to the role recently ascribed to EVs in conferring resistance and metastatic recurrence to anthracyclines[54]. In our model, once transferred from dying to viable cells, nucleic acids act as DAMPs leading to acute IFN-I production, which ultimaltely drives KDM1B-mediated cancer cell reprogramming, and thus therapy failure and tumor re-growth (**Figure 6h**). Two results support this IFN-I-KDM1B centered model. First, ICD-CSC enrichment was abrogated by inhibiting the ISG KDM1B, by ablating IFNAR signaling, or by depleting the entire (but not single) spectrum of self-nucleic acids. This latter result also suggests the existence of a certain degree of redundancy in, and compensation between, nucleic acid-sensing pathways, ensuring IFN-I production also when specific signals or sensors are depleted/missing. Second, by integrating ATAC-seq and RNA-seq analyses, we revealed extensive transcriptional reprogramming in ICD-CSCs, manifested with increased expression of genes related to stemness, invasiveness and metastatization coupled to silencing of tumor suppressor and immune stimulating genes.

Although further confirmation in human models is required, we hypothesize that activation of the IFN-I signaling directly stimulates CSCs in tumors undergoing ICD. We thus surmise the existence of a mechanism similar to that underlying virus-induced cell transdifferentiation which leads to the upregulation of core pluripotency genes[25]. Supporting our hypothesis, IFNs-I were recently ascribed to have a role in chromatin remodeling and gene expression reprogramming[39, 55]. Moreover, the expression of diverse KDMs has been correlated with “cold” TMEs in different tumor models, as also the use of epidrugs with the reinstatement of inflammation[56, 57, 58]. Recently, epidrug-related immune modulation was shown to co-occur with MYC suppression[59]. Moreover, our retrospective studies on BC patients that had received anthracycline based therapy showed signs of mutual correlation between *KDM1B*, IFN-I-related, stem-associated and IC metagenes, as well as the enrichment of CSCs along with immunogenic treatments. Further validation on a larger cohort of patients with patient follow-up will be launched.

In conclusion, we demonstrated that acute IFNs-I elicit a protective but ephemeral anticancer response. By triggering the ISG KDM1B, IFNs-I promote the appearance of heterogeneous CSCs, including CSCs with traits of immune privilege and therapy resistance. This evidence provides the basis for the use of epidrugs as adjunctives to anticancer immunogenic therapies, including conventional chemotherapies and current and upcoming immunotherapies, as a therapeutical means to prevent CSC expansion and patrol tumor recurrence.

Abbreviations

ABC, ATP-binding cassette; APM, antigen presentation machinery; ATAC-seq, assay for transposase-accessible chromatin using sequencing; ATCC, American Type Culture Collection; BC, breast cancer; BNZase, benzonase nuclease; CD44H, $CD133^{+}CD24^{+}CD44^{+high}$; CD44L, $CD133^{+}CD24^{+}CD44^{+low}$; CDDP, cisplatin; CSCs, cancer stem cells; cyto D, cytochalasin D; DAMPs, damage-associated molecular patterns; DOX, doxorubicin; DRFI, distant relapse-free incidence; DSS, disease-specific survival; EMT, epithelial-to-mesenchymal transition; EVs, extracellular vesicles; FACS, fluorescence activated cell sorting; IC, immune checkpoint; ICD, immunogenic cell death; ICD-CSCs, immunogenic cell death-induced CSCs; IFNs-I, Type I interferons; IFN-CSCs, Type I interferon-induced CSCs; IHC, immunohistochemistry; ISGs, interferon-stimulated genes; LRFI, local relapse-free incidence; MDR, multidrug resistance; MTX, mitoxantrone dihydrochloride; NSG, NOD SCID gamma; OVA, ovalbumin; OXP, oxaliplatin; PI, propidium iodide; qRT-PCR, quantitative RT-PCR; SP, side population; TCP, tranylcypromine; TF, transcription factor; TILs, tumor infiltrating lymphocytes; TME, tumor microenvironment; VRP, verapamil.

Declarations

Acknowledgments: We thank Paola Di Matteo, Roberto Ricci, Massimo Spada and Daniele Macchia for technical assistance, Dr. Enrico Proietti and Dr. Paola Sestili for providing IFNs-I, Pr. Laurence Zitvogel for providing MCA-derived clones, Dr. Oliver Kepp and Dr. Shuai Zhang for providing MCA-OVA, Dr. Ivan Tattoli for language and grammar editing. *In vivo* experiments were performed at Plaisant Castel Romano and Istituto Superiore di Sanità (Rome, Italy). This work was supported by the Associazione Italiana per la Ricerca sul Cancro (AIRC, Start-Up 2016 #18418) and Ministero Italiano della Salute (RF_GR-2013-02357273). IV is supported by the AIRC (IG 2017 grant number 20417) and a startup grant from the Italian Institute for Genomic Medicine (Candiolo, Turin, Italy) and Compagnia di San Paolo (Turin, Italy). GS is supported by the AIRC (IG 2018 grant number 21366). MHC is supported by the AIRC (IG 2019 grant number 16895). RDM is supported by the AIRC (5 × 1000 grant number 9979) and Ministero Italiano della Salute (RF_RF-2018-12367044)

Author Contributions: M.M. designed and performed experiments, analyzed and interpreted data and wrote the manuscript with the help of C.G., G.M., N.M.; A.G., M.S., M.P., M.P., M.F., M.H.C. analyzed data and performed bioinformatic studies; F.S. performed statistical analysis; A.D.B., C.E., E.P. performed IHC experiments and analysis; L.P. provided clinical data; A.D.N., L.B. designed and realized microfluidic systems; G.S., F.M., V.L. performed and analyzed experiments on microfluidic devices, F.F., S.R., G.Z.

performed and analyzed Luminex assay, M.S., A.B. analyzed flow cytometry data; L.B., E.A., S.V., M.B. designed experiments, I.V., A.S. obtained funding, supervised the project, designed experiments, analyzed data and wrote the manuscript; R.D.M. obtained funding, supervised the project, designed experiments and wrote the manuscript.

Author Disclosure: The authors have no conflicts of interest to disclose.

Methods

KEY RESOURCES TABLE

REAGENT or RESOURCE	SOURCE	IDENTIFIER
Antibodies		
Rat monoclonal anti-CD133 (13A4)	eBioscience™	Cat# 17-1331-81, RRID:AB_823120
Rat monoclonal anti-CD24 (M1/69)	eBioscience™	Cat# 12-0242-82, RRID:AB_465602
Rat monoclonal anti-CD44 (IM7)	eBioscience™	Cat# 11-0441-82, RRID:AB_465045
Rat monoclonal anti-CD8a (53-6.7)	eBioscience™	Cat# 17-0081-82, RRID:AB_469335
Rat monoclonal anti-CD273 (122)	eBioscience™	Cat# 11-9972-81, RRID:AB_465461
Mouse monoclonal anti-CD66a (CC1)	eBioscience™	Cat# 12-0661-80, RRID:AB_1311201
Mouse monoclonal anti-H2-K1 (AF6-88.5.5.3)	eBioscience™	Cat# 11-5958-80, RRID:AB_11151335
Rat monoclonal anti-CD274 (10F.9G2)	BioLegend®	Cat# 124312, RRID:AB_10612741
Rat monoclonal anti-Galectin-9 (108A2)	BioLegend®	Cat# 137903, RRID:AB_10568785
Rat monoclonal anti-CD366 (RMT3-23)	eBioscience™	Cat# 11-5870-82, RRID:AB_2688129
Rat monoclonal anti-CD45 (30-F11)	eBioscience™	Cat# MCD4528, RRID:AB_10373710
Mouse monoclonal anti-CD133/1 (AC133)	Miltenyi Biotec	Cat# 130-113-106
Recombinant monoclonal anti-CD44 (REA690)	Miltenyi Biotec	Cat# 130-113-342
Mouse monoclonal anti-CD24 (ML5)	BD Biosciences	Cat# BBA13, RRID:AB_356935
Mouse monoclonal anti-CD44v6 (2F10)	R&D Systems	Cat# BBA13, RRID:AB_356935
Rabbit polyclonal anti-MX1	Sigma-Aldrich	Cat# HPA049724, RRID:AB_2680862
Rabbit monoclonal anti-CD44 (SP37)	Sigma-Aldrich	Cat# SAB5500068
Mouse monoclonal anti-CD24 (SN3b)	Agilent Technologies	Cat# CBL561, RRID:AB_11212454
Mouse monoclonal anti-CD45 (2B11+PD7/26)	Agilent Technologies	Cat# GA75161-2, RRID:AB_2661839
Goat aniti-mouse Alexa Fluor® Plus 488	Thermo Scientific	Cat# A32723
Chemicals, Peptides, and Recombinant Proteins		
Purified mouse IFN-α/β and mock	Dr. E. Proietti, Istituto Superiore di Sanità, Rome	
Recombinant human Roferon-A®	Hoffmann-La Roche Ltd	
Cisplatin	Sigma-Aldrich	Cat# P4394
Doxorubicin hydrochloride	Sigma-Aldrich	Cat# D1515
Mitoxantrone dihydrochloride	Sigma-Aldrich	Cat# M6545
Oxaliplatin	Selleck Chemicals	Cat# S1224
Cytochalasin D	Sigma-Aldrich	Cat# C8273
Tranylcypromine	Calbiochem	Cat# 616431
Verapamil	Sigma-Aldrich	Cat# V4629
Benzonase nuclease	Sigma-Aldrich	Cat# E8263
DNase I	Qiagen	Cat# 79254

Ribonuclease A	Sigma-Aldrich	Cat# R6513
Ribonuclease H	Thermo Scientific	Cat# EN0201
Collagenase A	Sigma-Aldrich	Cat# COLLA-RO
Trypan Blue Stain (0.4%)	Thermo Scientific	Cat# 15250061
DMSO	Sigma-Aldrich	Cat# 5879
Hoechst 33342	Thermo Scientific	Cat# H1399
DAPI	Thermo Scientific	Cat# D1306
PI	Thermo Scientific	Cat# P1304MP
CFSE	Sigma-Aldrich	Cat# 21888
SeaPlaque GTG Agarose	Lonza	Cat# 50111
Ppia (Mm00620857_s1) primers	Applied Biosystems™	Cat# 4331182
Klf4 (Mm00516104_m1) primers	Applied Biosystems™	Cat# 4331182
Myc (Mm00487804_m1) primers	Applied Biosystems™	Cat# 4331182
Pou5f1 (Mm03053917_g1) primers	Applied Biosystems™	Cat# 4331182
Sox2 (Mm03053810_s1) primers	Applied Biosystems™	Cat# 4331182
Nanog (Mm02019550_s1) primers	Applied Biosystems™	Cat# 4331182
Hes1 (Mm01342805_m1) primers	Applied Biosystems™	Cat# 4331182
Nes (Mm00450205_m1) primers	Applied Biosystems™	Cat# 4331182
Twist1 (Mm00442036_m1) primers	Applied Biosystems™	Cat# 4331182
Snai1 (Mm00441533_g1) primers	Applied Biosystems™	Cat# 4331182
Cdh2 (Mm01162497_m1) primers	Applied Biosystems™	Cat# 4331182
Vim (Mm00619195_g1) primers	Applied Biosystems™	Cat# 4331182
Fn1 (Mm01256744_m1) primers	Applied Biosystems™	Cat# 4331182
Lgals9 (Mm00495295_m1) primers	Applied Biosystems™	Cat# 4331182
Pdcd1lg2 (Mm00451734_m1) primers	Applied Biosystems™	Cat# 4331182
Pdl1 (fw: GCATTATATTCACAGCCTGC, rw: CCCTTCAAAAGCTGGTCCTT) primers	Sigma-Aldrich	Custom
Agarose gel	Sigma-Aldrich	Cat# A9539
SYBR Safe DNA gel stain	Thermo Scientific	Cat# S33102

Crystal Violet	Sigma-Aldrich	Cat# C0775
Matrigel	BD Biosciences	Cat# 354234
PKH26 Red Fluorescent Cell Linker	Sigma-Aldrich	Cat# PKH26GL
CD45 MicroBeads	Miltenyi	Cat# 130-052-301
Agencourt AMPure SPRI beads	Beckman Coulter	Cat# A63880

Critical Commercial Assays		
RNeasy Plus Mini Kit	Qiagen	Cat# 74134
RNeasy Mini Kit	Qiagen	Cat# 74104
GoTaq® Probe 1-Step RT-qPCR System	Promega	Cat# A6120
Mouse magnetic Luminex screening assay CCL11/Eotaxin (BR74), CCL12/MCP-5 (BR42), CCL2/MCP-1/JE (BR18), CCL3/MIP-1α (BR46), CCL4/MIP-1β (BR51), CCL22/MDC (BR75), CCL8/MCP-2 (BR38), CXCL1/KC (BR13), CXCL10/IP-10 (BR37), CXCL12/SDF-1α (BR54), CXCL2/MIP-2 (BR20)	R&D Systems	Cat# LXSAMSM-12
Mouse pluripotent stem cell transcription factor analysis kit assayssing Nanog (M55-312)	BD Biosciences	Cat# 560585
CellTiter-Glo® Luminescent Cell Viability Assay	Promega	Cat# G7572
ExoEasy Maxi Kit	Qiagen	Cat# 76064
Nextera Library Prep Kit	Illumina	Cat# 20018704
MinElute PCR purification kit	Qiagen	Cat# 28004
KAPA Library Quantification Kit for Illumina platforms	KAPA Biosystems - Hoffmann - La Roche	Cat# KR0405
TruSeq Stranded mRNA Library kit	Illumina	Cat# 20020594
ChromoPlex TM1 Dual Detection	Bond III, Leica Biosystems	Cat# DS9665
Experimental Models: Cell Lines		
MCA205 mouse fibrosarcoma cell line		Cat#SCC173; RRID:CVCL_VR90
Panel of MCA-derived cancer cell clones	Pr. Laurence Zitvogel, Gustave Roussy cancer Campus, Villejuif	
MCA205-OVA mouse fibrosarcoma cell line	Dr. Oliver Kepp, Gustave Roussy cancer Campus, Villejuif	
AT3 mouse mammary carcinoma cell line	Sigma-Aldrich	Cat# SCC178, RRID:CVCL_VR89
CT26 WT mouse colon carcinoma cell line	ATCC	Cat# CRL-2638, RRID:CVCL_7256
B16.F10 murine melanoma cell line	ATCC	Cat# CRL-6475, RRID:CVCL_0159
MDA-MB-231 human breast carcinoma cell line	ATCC	Cat# HTB-26, RRID:CVCL_0062
U2OS human bone osteosarcoma cell line	ATCC	Cat# HTB-96, RRID:CVCL_0042
Experimental Models: Organisms/Strains		
Mouse: C57BL/6J	The Jackson Laboratory	Cat# 000664; RRID:IMSR_JAX:000664
Mouse : NOD.Cg-Prkdcscid Il2rgtm1Wjl/SzJ (NSG)	The Jackson	Cat# 005557;

	Laboratory	RRID:IMSR_JAX:005557
Mouse: C57BL/6-Tg(TcraTcrb)1100Mjb/Crl OT1	Charles River	Strain Code 642
Software and Algorithms		
Flowjo v10.0.7	Flowjo, LLC	RRID: SCR_008520
Illustrator CC 2015	Adobe Systems Inc.	RRID: SCR_010279
Photoshop CC 2015	Adobe Systems Inc.	RRID: SCR_014199
ImageJ	National Institute of Health	http://rsb.info.nih.gov/ij/; RRID: SCR_003070
Bio-Plex Manager Software version 6.1	Bio-Rad	RRID:SCR_014330
BWA algorithm		RRID:SCR_010910
STAR alignment – DESeq2 software		RRID:SCR_015687
“R” software	R Foundation for Statistical Computing	http://www.R-project.org/
HOMER software		RRID:SCR_010881
BiNGO software		
EnrichmentMap software		
GraphPad Prism	GraphPad Software	
Microsoft Excel	Microsoft, Redmond	RRID:SCR_016137
SPSS software	SPSS Inc.	
Other		
Roswell Park Memorial Institute 1640 (RPMI 1640)	EuroClone	Cat# ECB9006L
Dulbecco’s Modified Eagle Medium high glucose (DMEM)	EuroClone	Cat# ECB7501LX60
Fetal bovine serum (FBS)	EuroClone	Cat# ECS0180L
Penicillin G sodium salt and streptomycin sulfate	EuroClone	Cat# ECB3001D/1
L-glutamine 200 mM	EuroClone	Cat# ECB3004D
Dulbecco’s Modified Eagle Medium (DMEM)	Thermo Scientific	Cat# 52100047
Ham's F-12 Nutrient Mix (F-12)	Thermo Scientific	Cat# 21700018
Bovine serum albumin (BSA)	US Biological, Salem	Cat# A1312
Penicillin-Streptomycin-Amphotericin B (PSF)	Lonza	Cat# 17-745E
Sodium Bicarbonate 7.5% solution	Thermo Scientific	Cat# 25080094
Hepes buffer 1M	Thermo Scientific	Cat# 15630056
L-glutamine 200mM	Thermo Scientific	Cat# 25030024
Human apotransferrin	Sigma-Aldrich	Cat# T2252
Heparin sodium salt	Sigma-Aldrich	Cat# H3393
D-(+)-Glucose solution	Sigma-Aldrich	Cat# G8769
Recombinant human insulin	Sigma-Aldrich	Cat# 91077C
Progesterone	Sigma-Aldrich	Cat# P8783
Putrescine dihydrochloride	Sigma-Aldrich	Cat# P5780
Sodium selenite	Sigma-Aldrich	Cat# S5261

Recombinant human epidermal growth factor (EGF)	PeproTech Inc.	Cat# AF-100-15
Recombinant human fibroblast growth factor basic (bFGF)	PeproTech Inc.	Cat# AF-100-18B
Nicotinamide	Sigma-Aldrich	Cat# N0636
Trypsin-EDTA w/ Phenol Red	EuroClone	Cat# ECM0920
Dulbecco's Phosphate-Buffered Saline (D-PBS)	EuroClone	Cat# ECB4053L
Paraformaldehyde	Sigma-Aldrich	Cat# 158127
MACS columns	Miltenyi Biotec	Cat# 130-042-201, Cat# 130-042-401
MACS separators	Miltenyi Biotec	Cat# 130-042-109, Cat# 130-042-302

CONTACT FOR REAGENT AND RESOURCE SHARING

Further information and requests for resources and reagents should be directed to and will be fulfilled by the Lead Contact, Antonella Sistigu (antonella.sistigu@unicatt.it).

EXPERIMENTAL MODELS AND METHODS DETAILS

Cell lines and culture conditions. Unless otherwise indicated, plasticware was from Falcon, Corning B.V. Life Sciences (Corning, NY). MCA205 and MCA205-OVA mouse fibrosarcoma cell line, MCA205-derived clones (*Wt*, *Ifnar*$^{-/-}$, *Tlr3*$^{-/-}$, *Ticam*$^{-/-}$, *Ifih*$^{-/-}$, *Mavs*$^{-/-}$, *Sting1*$^{-/-}$, produced as reported in [18]), AT3 mouse mammary carcinoma and CT26 WT mouse colon carcinoma cell lines were cultured in a Roswell Park Memorial Institute 1640 (RPMI 1640) growth medium supplemented with 10% (v/v) fetal bovine serum (FBS), 2 mM L-glutamine, 100 IU/mL penicillin G sodium salt and 100 µg/mL streptomycin sulfate. B16.F10 murine melanoma cells, MDA-MB-231 human breast carcinoma cells and U2OS human bone osteosarcoma cells were cultured in Dulbecco's Modified Eagle Medium high glucose (DMEM) supplemented as above. All cell lines were maintained in standard culture conditions (37°C, 5% CO_2).

For testing the potential of induced cancer stem cells (CSCs) to growth under standard culture conditions already established for colorectal CSCs[60], we used the CSC medium described in [60]. In more details DMEM/F12-based culture medium was supplemented with 4 mg/mL bovine serum albumin (BSA), 1X Penicillin-Streptomycin-Amphotericin B (PSF), 0.13% NaHCO3, 6 mM Hepes, 2 mM L-glutamine, 0.1 mg/mL apotransferrin, 0.4 units heparin sodium salt, 1.1% glucose, 25 µg/mL insulin, 6.3 ng/mL progesterone, 9.7 µg/mL putrescine dihydrochloride, and 5.2 ng/mL sodium selenite and supplemented with 20 ng/mL human epidermal growth factor (EGF), 10 ng/mL human basic fibroblast growth factor (bFGF), and 10 mM nicotinamide. CSCs were passaged once/twice a week at dilution 1:2 by mechanical dissociation, through a micropipette, and incubated in standard culture conditions in ultra-low attachment tissue culture flasks.

Cytofluorometric analysis and cell sorting. To assess the expression of specific surface markers on putative-induced CSCs, 1 x 10^5 murine and human tumor cells were cultured in 6-well plates in 2 mL of growth medium and treated 72h with purified mouse IFN-α/β or recombinant human Roferon-A® (6000 U/mL) or with DOX (25 µM) or OXP (300 µM) alone or in combination with TCP (10 µM) for 48h. Cells

were then collected, washed in Dulbecco's Phosphate-Buffered Saline (D-PBS) and stained with fluorescently labeled mAbs directed against human/murine CD44, CD133 and/or CD24, or with purified-CD44v6 mAb, at optimal mAb concentrations (dilution 1:20, as previously determined by titration), in a cold D-PBS solution containing 1% FBS (D-PBS-FBS 1%). Samples were incubated in the dark on ice for 30min and then washed twice with cold D-PBS-FBS 1% solution. Thereafter, cells stained with CD44v6 mAb, were co-stained with the appropriate Alexa Fluor® 488 secondary Ab (diluted at 1:500 in D-PBS-FBS 1%) on ice for 30min. Cells were washed twice before the addition of 150 µL growth medium supplemented with 1 µg/mL DAPI. Sample acquisitions were performed by means of a BD FACSCanto™ II (BD Biosciences), MACSQuant® VYB Analyzer 10 (Miltenyi Biotec), or CytoFLEX (Beckman Counter) cytofluorometer, while data were analyzed by using the FlowJo software v10.0.7. By using the same procedure of costaining, specific CSC-like subsets (named ICD-CSCs or IFN-CSCs) were isolated by fluorescence activated cell sorting (FACS) by means of a BD FACSAria™ cytometer (BD Biosciences) and further characterized by *in vitro* and *in vivo* assays.

Other types of cell subsets were also sorted from MCA205 cells first treated with 2.5 µM DOX for 48h, and then FACS-isolated based on their low or high positivity for red fluorescence, named respectively DOX^{+low} and DOX^{+high} cells. For the assessment by flow cytometry of the expression of immune checkpoint molecules, FACS-isolated ICD-CSCs from AT3 and MCA205 cells were stained at 4°C for 30min in the dark with the following murine fluorochrome-conjugated mAbs directed against: PD-L1 (diluted at 1:100); PD-L2CD1LG (diluted at 1:100), LGALS9 (diluted at 1:20), CEACAM1 (diluted at 1:100) and H2-K1 (diluted at 1:50). DAPI was used to distinguish live and dead cells, and analysis of the expression of immune checkpoint molecules was made only in live cells. Samples were then analyzed by means of a MACSQuant® VYB cytofluorometer.

To evaluate how free nucleic acids contribute to the acquisition of CSC traits, 3 x 10^5 murine tumor cells were cultured in 6-well plates (2 mL of medium/well) and treated with 300 µM OXP for 24h (“donor” cells). Thereafter, “donor” cells were collected, washed from OXP and incubated at 37°C for up to 4h in 1,5 mL-eppendorf microtubes containing growth medium, supplemented or not, with 200 IU/mL BNZase, 10 IU/mL RNase A, 10 IU/mL RNase H or 100 IU/mL DNase. Next, such “donor cells” were cocultured with untreated live cells (“receiving” cells) for 24h in the presence or not of the indicated nucleases before cytofluorometric-mediated assessment of CSC surface markers on “receiving” cells.

Side-population (SP) assay. The detection of CSCs based on the Hoechst 33342 dye efflux [via the ATP binding cassette (ABC) transporter proteins] was performed as previously reported[61, 62]. Briefly, 1 x 10^5 murine tumor cells were cultured in 6-well plates (2 mL of medium/well) and treated with 6000 U/mL IFN-α/β for 72h, 30 µM OXP or 2.5 µM DOX for 48h. Cells were then collected, washed and incubated in pre-warmed growth medium in the presence or not of 100 µM VRP for 30min at 37°C. Five µg/mL Hoescht 33342 was added to cell suspension for 90min at 37°C in the dark. Data acquisition was performed using a MACSQuant® VYB cytometer. SP was identified as the distinct Hoechst 33342^- cell population (450-50 nm band-pass filter channel) within PI^- cells. Data were analyzed by using FlowJo software v10.0.7.

Quantitative (q)RT-PCR. Total RNA extraction and genomic DNA removal were performed with the RNeasy Plus Mini Kit following manufacturer's instructions. Total RNA (30 ng from each sample) was reverse transcribed and amplified using GoTaq® Probe 1-Step RT-qPCR System in the presence of specific primers and probes for murine genes, following manufacturer's instructions. The following primers were used : *Klf4* (Mm00516104_m1), *Myc (*Mm00487804_m1), *Pou5f1* (Mm03053917_g1), *Sox2* (Mm03053810_s1), *Nanog* (Mm02019550_s1), *Hes1* (Mm01342805_m1), *Nes* (Mm00450205_m1), *Twist1* (Mm00442036_m1,), *Snai1* (Mm00441533_g1), *Cdh2* (Mm01162497_m1), *Vim* (Mm00619195_g1), *Fn1* (Mm01256744_m1), *Lgals9* (Mm00495295_m1), *Pdcd1lg2* (Mm00451734_m1) and *Pdl1* (fw: GCATTATATTCACAGCCTGC, rw: CCCTTCAAAAGCTGGTCCTT). QRT-PCR was analyzed on a StepOnePlus Real-Time PCR System. qRT-PCR data were invariably normalized to the expression levels of the housekeeping gene *Ppia* (Mm00620857_s1).

Semiquantitative RT-PCR. Total RNA extraction and genomic DNA removal were performed as above. RT-PCR reaction was carried out, as indicated before in the qRT-PCR section, in the presence of the same specific primers and probes used for qRT-PCR. Amplified products were resolved by electrophoresis in 2% agarose gel and visualized by using SYBR Safe DNA gel staining.

Clonogenic assay. For assessing the clonogenicity of IFN-induced CSCs (referred to as IFN-CSCs), 1 x 10^3 IFN-α/β pre-treated cancer cells were seeded in 24-well plates between two layers consisting of 0.4% agarose for a final volume of 500 µL of growth medium supplemented as in [60] (CSC medium). Cells were incubated under standard culture conditions for up to 15 days. Colonies were then fixed/stained with 0.02% crystal violet (diluted in 20% methanol) and counted under an inverted microscope. Some of these spheres, prior to fixation, were recovered, cultured in ultra-low attachment flasks in CSC medium and analyzed for their morphology and transcriptional profiles.

Multidrug resistance assay. To determine CSC resistance to conventional chemotherapeutics, 5 x 10^3 parental and IFN-CSC MCA205 cells were seeded in 96-well plates (90 µL of medium/well) and either left untreated (“0”) or treated with growing doses of OXP (3-30-300 µM), DOX (0.25-2.5-25 µM) and MTX (0.04-0.4-4 µM) for 72h. Cell viability/proliferation was determined by luminescence counting of ATP levels in each well using the CellTiter-Glo® Luminescent Cell Viability Assay and a multimode reader (DTX-880; Beckman Coulter) according to manufacturer’s instructions.

T cell proliferation and cancer cell killing assays. MCA205-OVA were UV irradiated as in [63] and co-cultured with BM-derived DCs (differentiated as in [64]) at a 2:1 ratio for 24h. DCs were then cultured at a 5:1 ratio with splenic purified $CD8^+$ OT-1cells for 72h. Cross-primed $CD8^+$ OT-1 cells were then labelled with 1 µM CFSE dye (Sigma Aldrich) for 10min at 37°C, and re-stimulated with live parental or CD44L MCA205-OVA cells at 1:5 ratio. Three days later, cells were recovered and analyzed by flow cytometry (CytoFLEX, Beckman Coulter) for CFSE levels on live gated $CD8^+$ cells and PI levels on $CD45^-$ cells. Data were analyzed by using FlowJo software v10.0.7.

Microfluidic co-culture system for tumor-immune interactions. Microfluidic devices were fabricated in polydimethylsiloxane following well-established replica molding procedures[65]. Prior to cell loading, each device was sterilized under UV light in a laminar flow hood for 30min and then filled with RPMI 1640 growth medium and incubated for 1h at 37°C to equilibrate the system. To follow chemical and physical contacts between tumor cells and immune cells, parental AT3 cells, or their ICD-induced CSC counterparts (referred to as ICD-CSCs), were co-cultured with histocompatible H-2Kb splenocytes from C57BL/6J mice. Cells were loaded into the reservoirs of microfluidic devices as follows: the chambers were filled with 200 µl RPMI 1640 growth medium containing on one side 2 x 10^6 mouse splenocytes and on the other 5 x 10^4 tumor cells. Through an array of narrow micro-channels, immune cells can migrate toward tumor cells. Time-lapse recordings were carried out over a period of 72h by means of a Juli Smart microscope (Bulldog Bio Inc, Porthsmouth, NH) placed inside the incubator for all the duration of the recordings. The microscope generated 1 microphotograph every 2min, for a total of 720 images *per* day. Tracking analysis of timelapse microphotographs was performed by using the Manual Tracking plug-in of the ImageJ v1.5 software.

Microfluidic devices based on competition. To concomitantly confront the immune cells with different tumor cell populations, 2 x 10^4 parental AT3 cells and their ICD-CSC counterparts were resuspended on ice in 3 µL Matrigel (2 mg/mL), loaded in two opposite lateral chambers and mantained at 37°C for 30min to allow gel solidification. Then, 1 x 10^6 histocompatible splenocytes, labeled with live-compatible PKH26 Red Fluorescent Cell Linker following manufacturer's instructions, were loaded in the central chamber in 10 µl of RPMI 1640 growth medium[66, 67]. Phase-contrast, visible and fluorescence microphotographs were generated by using an EVOS-FL fluorescence microscope (Life Technologies – Thermo Scientific). Fluorescence analysis and image overlays were performed by using ImageJ v1.5 software.

Extracellular vesicle (EV) isolation and uptake. To assess the involvement of EV-carried nucleic acids in the induction of CSCs, 3 x 10^5 MCA205 cells were seeded in 6-well plates (2 mL of medium/well), treated with 300 µM OXP for 4h ("donor" cells) and then washed. Purification of EVs from cell culture supernatant was performed using exoEasy Maxi Kit following manufacturer's instructions. Isolated EVs were put on "receiving cells" for 24h in presence or not of the endocytosis inhibitor cytochalasin D (0.5 µM). "Receiving" cells were then analyzed by cytofluorometry and qRT-PCR. For uptake analysis, isolated EVs were labeled with the PKH26 Red Fluorescent Cell Linker, washed with Exosome Spin Columns (Cat# 4484449, Invitrogen – Thermo Scientific) and co-cultured for 4h with "receiving" cells either at 37°C or 4°C. Thereafter, cells were washed, fixed in 4% (w/v) paraformaldehyde in D-PBS, and analyzed by flow cytometry and EVOS-FL fluorescence microscope.

Luminex assay. To evaluate the basal differences in chemokine patterns, parental MCA205 cells, parental AT3 cells and their respective ICD-CSC counterparts were seeded in 24-well plates (1 mL medium/well) and grown for 48h. Supernatants were collected on ice, centrifuged and immediately freezed at -80°C. Chemokines were measured by a xMAP multiplex technology using a Mouse Magnetic Luminex assay

multiplex panel including the following molecules: CCL2/MCP-1/JE; CCL3/MIP-1α; CCL4/MIP-1β; CCL5/RANTES; CCL8/MCP-2; CCL11/Eotaxin; CCL12/MCP-5; CCL22/MDC; CXCL1/KC; CXCL2/MIP-2; CXCL10/IP-10; CXCL12/SDF-1α. The analysis was performed by using 50 µL of 2-fold diluted samples. The quantification was carried out on a Bio-Plex® 200 System (Bio-Rad, Hercules, CA) equipped with a magnetic workstation and a Bio-Plex Manager Software version 6.1 and results were expressed as pg/mL. The level of each detected molecule was normalized to the total cell number.

Assay for transposase-accessible chromatin using sequencing (ATAC-seq). To investigate chromatin accessibility dynamics, 1 x 10^5 parental MCA205 cells and their IFN-CSC counterparts were treated with DNase I at 37°C for 30min. Cells were then washed and cryopreserved in culture medium containing FBS and 5% DMSO in 1,5 mL eppendorf microtubes. Cryopreserved cells were sent to Epigenetics Services Active Motif, Inc. (Carlsband, CA) to perform the ATAC-seq assay. Cells were thawed in a 37°C water bath, pelleted, washed with cold PBS, and tagmented as previously described[68], with some modifications based on [69]. Briefly, cell pellets were resuspended in lysis buffer, pelleted, and tagmented using the enzyme and buffer provided in the Nextera Library Prep Kit. Tagmented DNA was then purified using the MinElute PCR purification kit, amplified with 10 cycles of PCR, and purified using Agencourt AMPure SPRI beads. Resulting material was quantified using the KAPA Library Quantification Kit for Illumina platforms, and sequenced with PE42 sequencing on the NextSeq 500 sequencer (Illumina). Analysis of ATAC-seq data was performed as follows. Reads were aligned to the mouse genome (mm10) using the BWA algorithm. Duplicate reads were removed, only reads mapping as matched pairs and only uniquely mapped reads (mapping quality ≥1) were used for further analysis. Alignments were extended *in silico* at their 3'-ends to a length of 200 bp and assigned to 32-nt bins along the genome. The resulting histograms (genomic "signal maps") were stored in bigWig files. Peaks were identified using the MACS 2.1.0 algorithm at a cutoff of p-value 1e-7, without control file, and with the –nomodel option. Peaks that were on the ENCODE blacklist of known false ChIP-Seq peaks were removed. Signal maps and peak locations were used as input data to Active Motifs proprietary analysis program, which creates Excel tables containing detailed information on sample comparison, peak metrics, peak locations and gene annotations. A peak re-calling strategy was used to reduce false positives as previously done in [70].

RNA-seq. To determine the overall transcriptional profile, 2.5 x 10^5 parental MCA205 cells and their IFN-CSC counterparts were harvested, washed and cryopreserved in 1,5 mL eppendorf microtubes. As above, RNA-seq analysis was performed by Epigenetics Services Active Motif, Inc. Total RNA was isolated from cells by using the RNeasy Mini Kit. For each sample, 2 µg of total RNA was then used in Illumina's TruSeq Stranded mRNA Library kit. Libraries were sequenced on Illumina NextSeq 500 as paired-end 42-nt reads. Sequence reads were analyzed with the STAR alignment – DESeq2 software pipeline described in the Data Explanation document.

Transcription factor motif discovery and network analysis. Motif enrichment analysis was performed using the HOMER software comparing the motifs enriched in the target set (*i.e.*, the *loci* obtained from ATAC-Seq analysis) with those of reference (*i.e.*, randomly selected background sequences). Only motif

ratios ≥2 with *P*-value (Benjamini-Hochberg correction) ≤0.05 were considered biologically and statistically significant. The functional enrichment analysis was performed by using the clusterProfiler package as in [71]. Network visualizations were made by using the enrichPlot package.

Animals. Mice were maintained in specific pathogen–free conditions in a temperature-controlled environment with 12h light - 12h dark cycles and received food and water *ad libitum*. All the *in vivo* experimentations were in compliance with the EU Directive 63/2010 and included in an experimental protocol approved by the Institutional Animal Experimentation Committee (858/2015-PR). Six-to-7 week-old female C57Bl/6J, and NOD SCID gamma (NSG) mice were purchased from Jackson Laboratory, C57BL/6-Tg(TcraTcrb)1100Mjb/J OT1 mice were from Charles River, housed in the animal facility at the Istituto Superiore di Sanità and employed after an acclimatization period of 7 days. All experiments were randomized and blinded and sample sizes were calculated to detect a statistically significant effect.

Tumor models, vaccination and chemotherapy. To assess cancer cell tumorigenic capacity, 1 x 10^2; 1 x 10^3; 1 x 10^4; 1 x 10^5 parental MCA205 and and their IFN-CSC counterparts were subcutaneously inoculated into the flank of C57Bl/6J and NSG mice. Tumor surface (longest dimension x perpendicular dimension) was routinely monitored using a common caliper. For vaccination experiments, 1 x 10^5 parental MCA205 cells were subcutaneously inoculated in mice which rejected the first injection, and tumor growth was monitored weekly. The absence of tumors was considered an indication of efficient antitumor vaccination.

To *in vivo* uncover the ability of immunogenic chemotherapy to induce CSC appearance and to test IFN-CSC therapy response, 1 x 10^6 parental or IFN-CSC MCA205 were subcutaneously inoculated into the flank of C57Bl/6J mice and tumor growth was weekly monitored (as above described). When the tumor surface reached 35–45 mm^2 mice were randomized to control and treatment groups (10 mice/group) and injected with either CDDP (2.5 mg/kg) or DOX (2.9 mg/kg), both intratumorally in 50 µl of D-PBS, TCP (5 mg/kg) intraperitoneally every 3 days alone, a combination of DOX+TCP, or 50 µl of D-PBS intratumorally. All experiments contained 5 to 10 mice per group and were run at least 2 times, yielding similar results. All data were analyzed by using GraphPad Prism.

Tumor dissection, flow cytometry and sorting. Tumors from mice either treated with CDDP, DOX, D-PBS, TCP, DOX+TCP were carefully removed 15 days after treatment. Tumor burdens were cut into small pieces with scissors within digesting buffer (400 U/ml Collagenase A and 200 U/ml DNase I in RPMI 1640) and incubated for 30min at 37°C. Single cell suspensions obtained by grinding the digested tissue and filtering them through a 70-µm cell strainer were then purified based on CD45 expression, by using mouse CD45 MicroBeads, MACS columns and separators (used following manufacter's recommandations). After washing with D-PBS, $CD45^+$ cells, uncluding tumor infiltrating lymphocytes (TILs), were resuspended at 1 x 10^7 cells/mL and stained at 4°C for 30min in the dark with the following murine-specific fluorochrome-conjugated mAbs directed against: CD45 (diluted at 1:25); CD8a (diluted at 1:150); and TIM-3 (diluted at 1:100). Similarly, the $CD45^-$ cellular fraction (including tumor cells) was stained as

follows: CD45, CD133, CD44, CD24 and Nanog (diluted at 1:5). DAPI was used to distinguish live and dead cells and only live cells were included in the analysis. Samples were then analysed by means of a MACSQuant® VYB or a CytoFLEX cytofluorometer.

***In vivo* invasiveness assay.** For invasiveness studies, 2 x 10^5 parental MCA205 cells and their ICD-CSCs counterparts were intravenously injected into the tail of C57Bl/6J mice. Fiftheen days post injection, lungs were explanted and macrometastases were counted. Images of lung metastases were captured by using a ZEISS STEMI 305 Stereo microscope (Carl Zeiss, Oberkochen, Germany). All experiments contained 5 to 10 mice per group and were run at least 2 times, yielding similar results. All data were analyzed by using GraphPad Prism.

Immunohistochemistry (IHC). Three-micrometer sections of formalin-fixed paraffin embedded breast cancer (BC) biopsies and autologous surgery tissues were cut on SuperFrost Plus slides (Menzel-Gläser, Braunschweig, Germany). Immunoreactions against CD45 and MX1 were revealed by Bond Polymer Refine Detection in an automated autostainer (Bond III, Leica Biosystems, Wetzlar, Germany) using the following antibodies: anti-mouse CD45 mAb (clone 2B11, dilution of 1:100, pH 6) and anti-rabbit MX1 polyclonal Ab (dilution of 1:100, pH 6). Diaminobenzidine was used as chromogenic substrate. The immunohistochemical assessment of CD44 and CD24 was performed with ChromoPlex TM1 Dual Detection in an automated autostainer by using an anti-rabbit CD44 mAb (clone SP37, dilution of 1:150, pH 6) and anti-mouse CD24 mAb (clone SN3, dilution of 1:500, pH 8). Diaminobenzidine and Fast Red were used as chromogenic substrates. Immunoreactions were scored independently by 2 investigators (CE and ADB). Blinded to treatment outcomes and discordant cases were reviewed for the final assessment.

Patients included in neoadjuvant chemotherapy studies. For IHC retrospective analyses 20 patients, with histologically confirmed BC by the Pathology Unit at the Regina Elena National Cancer Institute (Rome), were included. All the patients underwent biopsies and received anthracycline-based neoadjuvant chemotherapy. For metagene correlation analyses, the publicly available patient cohorts (accession codes GSE6861, GSE20271, GSE25065, GSE16446, GSE41998 and GSE32646) reported in [18, 37] were selected. In these studies gene expression analyses were performed on tumor biopsies obtained at diagnosis.

Statistical Analysis. Unless otherwise specified, all experiments were performed in triplicate parallel instances and independently repeated at least three times. Shapiro-Wilk Normality Test on SPSS software Version_21 was used to assess the presence or not of parametric distributions. According to these results, statistical significance of data from most *in vitro* and *in vivo* studies was evaluated by: (*i*) unpaired *t* test with Welch's correction; (*ii*) Mann-Whitney non-parametric test, (*iii*) ordinary one- or two-way ANOVA with Bonferroni's correction. The rate of migration of splenocytes into microfluidic devices was analyzed by two-way repeated measures ANOVA. For *in vivo* studies, the Log-rank (Mantel-Cox) test was applied to compare tumor growth curves. For IHC analyses, the Spearman's correlation coefficient was calculated to

assess the correlation between MX1 and CD44, CD24 markers. *P* values<0.05 were considered statistically significant.

References

1. Gottesman, M.M. Mechanisms of cancer drug resistance. *Annu Rev Med* **53**, 615-627 (2002).
2. Russo, M. *et al.* Adaptive mutability of colorectal cancers in response to targeted therapies. *Science* (2019).
3. Gatenby, R.A. & Brown, J.S. Integrating evolutionary dynamics into cancer therapy. *Nature reviews. Clinical oncology* **17**, 675-686 (2020).
4. Gilbert, L.A. & Hemann, M.T. DNA damage-mediated induction of a chemoresistant niche. *Cell* **143**, 355-366 (2010).
5. Lagadec, C., Vlashi, E., Della Donna, L., Dekmezian, C. & Pajonk, F. Radiation-induced reprogramming of breast cancer cells. *Stem Cells* **30**, 833-844 (2012).
6. Dahan, P. *et al.* Ionizing radiations sustain glioblastoma cell dedifferentiation to a stem-like phenotype through survivin: possible involvement in radioresistance. *Cell Death Dis* **5**, e1543 (2014).
7. Lu, H. *et al.* Chemotherapy-Induced Ca(2+) Release Stimulates Breast Cancer Stem Cell Enrichment. *Cell Rep* **18**, 1946-1957 (2017).
8. Dean, M., Fojo, T. & Bates, S. Tumour stem cells and drug resistance. *Nature reviews. Cancer* **5**, 275-284 (2005).
9. Batlle, E. & Clevers, H. Cancer stem cells revisited. *Nature medicine* **23**, 1124-1134 (2017).
10. Vitale, I., Shema, E., Loi, S. & Galluzzi, L. Intratumoral heterogeneity in cancer progression and response to immunotherapy. *Nature medicine* **27**, 212-224 (2021).
11. Cao, J. & Yan, Q. Cancer Epigenetics, Tumor Immunity, and Immunotherapy. *Trends in cancer* **6**, 580-592 (2020).
12. Wainwright, E.N. & Scaffidi, P. Epigenetics and Cancer Stem Cells: Unleashing, Hijacking, and Restricting Cellular Plasticity. *Trends in cancer* **3**, 372-386 (2017).
13. Cheng, Y. *et al.* Targeting epigenetic regulators for cancer therapy: mechanisms and advances in clinical trials. *Signal transduction and targeted therapy* **4**, 62 (2019).
14. Dawson, M.A. & Kouzarides, T. Cancer epigenetics: from mechanism to therapy. *Cell* **150**, 12-27 (2012).
15. Topper, M.J., Vaz, M., Marrone, K.A., Brahmer, J.R. & Baylin, S.B. The emerging role of epigenetic therapeutics in immuno-oncology. *Nature reviews. Clinical oncology* **17**, 75-90 (2020).
16. Villanueva, L., Alvarez-Errico, D. & Esteller, M. The Contribution of Epigenetics to Cancer Immunotherapy. *Trends in immunology* **41**, 676-691 (2020).
17. Schiavoni, G. *et al.* Cyclophosphamide synergizes with type I interferons through systemic dendritic cell reactivation and induction of immunogenic tumor apoptosis. *Cancer Res* **71**, 768-778 (2011).

18. Sistigu, A. *et al.* Cancer cell-autonomous contribution of type I interferon signaling to the efficacy of chemotherapy. *Nature medicine* **20**, 1301-1309 (2014).
19. Galluzzi, L., Buque, A., Kepp, O., Zitvogel, L. & Kroemer, G. Immunogenic cell death in cancer and infectious disease. *Nat Rev Immunol* **17**, 97-111 (2017).
20. Galluzzi, L. *et al.* Molecular mechanisms of cell death: recommendations of the Nomenclature Committee on Cell Death 2018. *Cell Death Differ* **25**, 486-541 (2018).
21. Musella, M., Manic, G., De Maria, R., Vitale, I. & Sistigu, A. Type-I-interferons in infection and cancer: Unanticipated dynamics with therapeutic implications. *Oncoimmunology* **6**, e1314424 (2017).
22. Hugo, W. *et al.* Genomic and Transcriptomic Features of Response to Anti-PD-1 Therapy in Metastatic Melanoma. *Cell* **165**, 35-44 (2016).
23. Benci, J.L. *et al.* Opposing Functions of Interferon Coordinate Adaptive and Innate Immune Responses to Cancer Immune Checkpoint Blockade. *Cell* **178**, 933-948 e914 (2019).
24. Dunn, G.P. *et al.* A critical function for type I interferons in cancer immunoediting. *Nature immunology* **6**, 722-729 (2005).
25. Lee, J. *et al.* Activation of innate immunity is required for efficient nuclear reprogramming. *Cell* **151**, 547-558 (2012).
26. Fang, R. *et al.* Human LSD2/KDM1b/AOF1 regulates gene transcription by modulating intragenic H3K4me2 methylation. *Molecular cell* **39**, 222-233 (2010).
27. Al-Hajj, M., Wicha, M.S., Benito-Hernandez, A., Morrison, S.J. & Clarke, M.F. Prospective identification of tumorigenic breast cancer cells. *Proc Natl Acad Sci U S A* **100**, 3983-3988 (2003).
28. Bocci, F. *et al.* Toward understanding cancer stem cell heterogeneity in the tumor microenvironment. *Proc Natl Acad Sci U S A* **116**, 148-157 (2019).
29. Marine, J.C., Dawson, S.J. & Dawson, M.A. Non-genetic mechanisms of therapeutic resistance in cancer. *Nature reviews. Cancer* **20**, 743-756 (2020).
30. Balkwill, F. Cancer and the chemokine network. *Nature reviews. Cancer* **4**, 540-550 (2004).
31. Acharyya, S. *et al.* A CXCL1 paracrine network links cancer chemoresistance and metastasis. *Cell* **150**, 165-178 (2012).
32. Wiedemann, G.M. *et al.* Cancer cell-derived IL-1alpha induces CCL22 and the recruitment of regulatory T cells. *Oncoimmunology* **5**, e1175794 (2016).
33. Vacchelli, E. *et al.* Chemotherapy-induced antitumor immunity requires formyl peptide receptor 1. *Science* **350**, 972-978 (2015).
34. Dixon, G. *et al.* QSER1 protects DNA methylation valleys from de novo methylation. *Science* **372** (2021).
35. Lu, H. *et al.* Chemotherapy-induced S100A10 recruits KDM6A to facilitate OCT4-mediated breast cancer stemness. *The Journal of clinical investigation* **130**, 4607-4623 (2020).
36. Zhang, W. *et al.* Targeting KDM4A epigenetically activates tumor-cell-intrinsic immunity by inducing DNA replication stress. *Molecular cell* (2021).

37. Hollern, D.P. *et al.* B Cells and T Follicular Helper Cells Mediate Response to Checkpoint Inhibitors in High Mutation Burden Mouse Models of Breast Cancer. *Cell* **179**, 1191-1206 e1121 (2019).
38. Barrat, F.J., Crow, M.K. & Ivashkiv, L.B. Interferon target-gene expression and epigenomic signatures in health and disease. *Nature immunology* **20**, 1574-1583 (2019).
39. Park, S.H. *et al.* Type I interferons and the cytokine TNF cooperatively reprogram the macrophage epigenome to promote inflammatory activation. *Nature immunology* **18**, 1104-1116 (2017).
40. Zitvogel, L., Galluzzi, L., Kepp, O., Smyth, M.J. & Kroemer, G. Type I interferons in anticancer immunity. *Nat Rev Immunol* **15**, 405-414 (2015).
41. Bracci, L., Sistigu, A., Proietti, E. & Moschella, F. The added value of type I interferons to cytotoxic treatments of cancer. *Cytokine Growth Factor Rev* **36**, 89-97 (2017).
42. Doherty, M.R. *et al.* Interferon-beta represses cancer stem cell properties in triple-negative breast cancer. *Proc Natl Acad Sci U S A* **114**, 13792-13797 (2017).
43. Castiello, L. *et al.* Disruption of IFN-I Signaling Promotes HER2/Neu Tumor Progression and Breast Cancer Stem Cells. *Cancer Immunol Res* **6**, 658-670 (2018).
44. Zhu, Y. *et al.* Influence of interferon-alpha on the expression of the cancer stem cell markers in pancreatic carcinoma cells. *Exp Cell Res* **324**, 146-156 (2014).
45. Qadir, A.S. *et al.* CD95/Fas Increases Stemness in Cancer Cells by Inducing a STAT1-Dependent Type I Interferon Response. *Cell Rep* **18**, 2373-2386 (2017).
46. Li, S. *et al.* Interferon alpha-inducible protein 27 promotes epithelial-mesenchymal transition and induces ovarian tumorigenicity and stemness. *J Surg Res* **193**, 255-264 (2015).
47. Meacham, C.E. & Morrison, S.J. Tumour heterogeneity and cancer cell plasticity. *Nature* **501**, 328-337 (2013).
48. Turajlic, S., Sottoriva, A., Graham, T. & Swanton, C. Resolving genetic heterogeneity in cancer. *Nat Rev Genet* **20**, 404-416 (2019).
49. Maccalli, C., Volonte, A., Cimminiello, C. & Parmiani, G. Immunology of cancer stem cells in solid tumours. A review. *Eur J Cancer* **50**, 649-655 (2014).
50. Miao, Y. *et al.* Adaptive Immune Resistance Emerges from Tumor-Initiating Stem Cells. *Cell* **177**, 1172-1186 e1114 (2019).
51. Jacquelot, N. *et al.* Sustained Type I interferon signaling as a mechanism of resistance to PD-1 blockade. *Cell Res* (2019).
52. Chen, J. *et al.* Type I IFN protects cancer cells from CD8+ T cell-mediated cytotoxicity after radiation. *The Journal of clinical investigation* **129**, 4224-4238 (2019).
53. Fan, J.B. *et al.* Type I Interferon Regulates a Coordinated Gene Network to Enhance Cytotoxic T Cell-Mediated Tumor Killing. *Cancer Discov* (2020).
54. Keklikoglou, I. *et al.* Chemotherapy elicits pro-metastatic extracellular vesicles in breast cancer models. *Nat Cell Biol* **21**, 190-202 (2019).

55. Wu, X. *et al.* Intrinsic Immunity Shapes Viral Resistance of Stem Cells. *Cell* **172**, 423-438 e425 (2018).
56. Sheng, W. *et al.* LSD1 Ablation Stimulates Anti-tumor Immunity and Enables Checkpoint Blockade. *Cell* **174**, 549-563 e519 (2018).
57. Qin, Y. *et al.* Inhibition of histone lysine-specific demethylase 1 elicits breast tumor immunity and enhances antitumor efficacy of immune checkpoint blockade. *Oncogene* **38**, 390-405 (2019).
58. Wu, L. *et al.* KDM5 histone demethylases repress immune response via suppression of STING. *PLoS biology* **16**, e2006134 (2018).
59. Topper, M.J. *et al.* Epigenetic Therapy Ties MYC Depletion to Reversing Immune Evasion and Treating Lung Cancer. *Cell* **171**, 1284-1300 e1221 (2017).
60. Manic, G. *et al.* CHK1-targeted therapy to deplete DNA replication-stressed, p53-deficient, hyperdiploid colorectal cancer stem cells. *Gut* **67**, 903-917 (2018).
61. Golebiewska, A., Brons, N.H., Bjerkvig, R. & Niclou, S.P. Critical appraisal of the side population assay in stem cell and cancer stem cell research. *Cell Stem Cell* **8**, 136-147 (2011).
62. Telford, W.G. Stem cell side population analysis and sorting using DyeCycle violet. *Curr Protoc Cytom* **Chapter 9**, Unit9 30 (2010).
63. Lorenzi, S. *et al.* Type I IFNs control antigen retention and survival of CD8alpha(+) dendritic cells after uptake of tumor apoptotic cells leading to cross-priming. *Journal of immunology* **186**, 5142-5150 (2011).
64. Roney, K. Bone Marrow-Derived Dendritic Cells. *Methods in molecular biology* **1960**, 57-62 (2019).
65. Businaro, L. *et al.* Cross talk between cancer and immune cells: exploring complex dynamics in a microfluidic environment. *Lab Chip* **13**, 229-239 (2013).
66. Lucarini, V. *et al.* Combining Type I Interferons and 5-Aza-2'-Deoxycitidine to Improve Anti-Tumor Response against Melanoma. *J Invest Dermatol* **137**, 159-169 (2017).
67. Parlato, S. *et al.* 3D Microfluidic model for evaluating immunotherapy efficacy by tracking dendritic cell behaviour toward tumor cells. *Sci Rep* **7**, 1093 (2017).
68. Buenrostro, J.D., Giresi, P.G., Zaba, L.C., Chang, H.Y. & Greenleaf, W.J. Transposition of native chromatin for fast and sensitive epigenomic profiling of open chromatin, DNA-binding proteins and nucleosome position. *Nat Methods* **10**, 1213-1218 (2013).
69. Corces, M.R. *et al.* An improved ATAC-seq protocol reduces background and enables interrogation of frozen tissues. *Nat Methods* **14**, 959-962 (2017).
70. Li, D. *et al.* Chromatin Accessibility Dynamics during iPSC Reprogramming. *Cell Stem Cell* **21**, 819-833 e816 (2017).
71. Yu, G., Wang, L.G., Han, Y. & He, Q.Y. clusterProfiler: an R package for comparing biological themes among gene clusters. *Omics : a journal of integrative biology* **16**, 284-287 (2012).

List Of Genes And Proteins

Actb, actin, beta [*Mus musculus*]; Aldh/Aldh3a1, aldehyde dehydrogenase family 3, subfamily A1 [*Mus musculus*]; Aldh5a1, aldhehyde dehydrogenase family 5, subfamily A1 [*Mus musculus*]; ANXA1, annexin A1 [*Mus musculus*]; Atf1, activating transcription factor 1 [*Mus musculus*]; Atf4, activating transcription factor 4 [*Mus musculus*]; Atp2a3, ATPase, Ca++ transporting, ubiquitous [*Mus musculus*]; Baiap2, brain-specific angiogenesis inhibitor 1-associated protein 2 [*Mus musculus*]; Bcl11a, B cell CLL/lymphoma 11A (zinc finger protein) [*Mus musculus*]; CCL2, chemokine (C-C motif) ligand 2 [*Homo sapiens*]; CCL22, chemokine (C-C motif) ligand 22 [*Mus musculus*]; CCL5, chemokine (C-C motif) ligand 5 [*Mus musculus*]; CD24, CD24 antigen [*Mus musculus*]; CD24, CD24 molecule [*Homo sapiens*]; Cd274/Pdl1, CD274 antigen [*Mus musculus*]; CD274/PD-L1, CD274 molecule/programmed death-ligand 1 [*Homo sapiens*]; CD44, CD44 antigen [*Mus musculus*]; CD44, CD44 molecule (Indian blood group) [*Homo sapiens*]; Cdh1, cadherin 1 [*Mus musculus*]; Cdh16, cadherin 16 [*Mus musculus*]; Cdh2, cadherin 2 [*Mus musculus*]; Cdk2ap1, CDK2 (cyclin-dependent kinase 2)-associated protein 1 [*Mus musculus*]; CEACAM1/CD66a, carcinoembryonic antigen-related cell adhesion molecule 1 [*Mus musculus*]; cGAS, cyclic GMP-AMP synthase [*Mus musculus*]; Csf1r, colony stimulating factor 1 receptor [*Mus musculus*]; CTCF, CCCTC-binding factor [*Mus musculus*]; Ctsl, cathepsin L [*Mus musculus*]; CXCL1, chemokine (C-X-C motif) ligand 1 [*Mus musculus*]; CXCL10, C-X-C motif chemokine ligand 10 [*Homo sapiens*]; CXCL2, chemokine (C-X-C motif) ligand 2 [*Mus musculus*]; DDX58, DEAD (Asp-Glu-Ala-Asp) box polypeptide 58 [*Mus Musculus*]; Dlg2, discs large MAGUK scaffold protein 2 [*Mus musculus*]; DLL3, delta like canonical Notch ligand 3 [*Homo sapiens*]; EBF, early B cell factor [*Mus musculus*]; Epb4.1/1, erythrocyte membrane protein band 4.1[*Mus musculus*]*;* Ets1, E26 avian leukemia oncogene 1, 5' domain [*Mus musculus*]; Fank, fibronectin type 3 and ankyrin repeat domains 1 [*Mus musculus*]; Fbxw2, F-box and WD-40 domain protein 2 [*Mus musculus*]; Fn1, fibronectin [*Mus musculus*]; FOX, Forkhead box [*Mus musculus*]; Gapdh, glyceraldheyde-3-phosphate dehydrogenase [*Mus musculus*]; Gata6, GATA binding protein 6 [*Mus musculus*]; Gpr17, G protein-coupled receptor 17 [*Mus musculus*]; Gsdmd, gasdermin D [*Mus musculus*]; H2-K1, histocompatibility 2, K1, K region [*Mus musculus*]; HAVCR2/CD366, Hepatitis A virus cellular receptor 2 [*Mus musculus*]; HES1, hes family bHLH transcription factor 1 [*Homo sapiens*]; Hes1, hes family bHLH transcription factor 1 [*Mus musculus*]; Hes2, hes family bHLH transcription factor 2 [*Mus musculus*]; HMGB1, high mobility group box 1 [*Mus musculus*]; Hnf1b,HNF1 homeobox N [*Mus musculus*]; IFI27, interferon alpha inducible protein 27 [*Homo sapiens*]; Ifi27l2a, interferon, alpha-inducible protein 27 like 2A [*Mus musculus*]; Ifi27l2b, interferon, alpha-inducible protein 27 like 2B [*Mus musculus*]; Ifih1, interferon induced with helicase C domain 1 [*Mus musculus*]; Ifnar1, interferon (alpha and beta) receptor 1 [*Mus musculus*]; IFNB1, interferon beta 1 [*Homo sapiens*]; Il12b, interleukin 12b [*Mus musculus*]; Il16, interleukin 16 [*Mus musculus*]; Il24, interleukin 24 [*Mus musculus*]; Il27, interleukin 27 [*Mus musculus*]; IRF, interferon regulatory factor [*Mus musculus*]; Itga5, integrin alpha 5 (fibronectin receptor alpha) [*Mus musculus*]; Jun/AP1, jun proto-oncogene [*Mus musculus*]; Kdm1b, lysine (K)-specific demethylase 1B [*Mus musculus*]; KDM1B, lysine demethylase 1B [*Homo sapiens*]; Klf4, Kruppel-like factor 4 (gut) [*Mus musculus*]; KLF4, Kruppel-like factor 4 [*Homo sapiens*]; Krt, keratin [*Mus musculus*]; LGALS9, lectin, galactose binding, soluble 9 [*Mus musculus*]; LGR5, leucine-rich repeat containing G protein-coupled receptor 5 [*Homo sapiens*]; MafB, v-maf musculoaponeurotic fibrosarcoma oncogene family, protein B (avian) [*Mus musculus*]; MafK, v-maf musculoaponeurotic fibrosarcoma oncogene family, protein K

(avian) [*Mus musculus*]; MAVS, mitochondrial antiviral signaling protein [*Mus musculus*]; Mtor, mechanistic target of rapamycin kinase [*Mus musculus*]; MX1, MX dynamin like GTPase 1 [*Homo sapiens*]; Myc myelocytomatosis oncogene [*Mus musculus*]; MYC, MYC proto-oncogene, bHLH transcription factor [*Homo sapiens*]; Myct1, myc target 1 [*Mus musculus*]; NANOG, Nanog homeobox [*Homo sapiens*]; Nanog, Nanog homeobox [*Mus musculus*]; Ncam/Ncam1, neural cell adhesion molecule 1 [*Mus musculus*]; NES, nestin [*Homo sapiens*]; Nes, nestin [*Mus musculus*]; NF1, neurofibromin 1 [*Mus musculus*]; NFAT, Nuclear factor of activated T-cells [*Mus musculus*]; NFKB1/NFkB-p50, nuclear factor of kappa light polypeptide gene enhancer in B cells 1, p105 [*Mus musculus*]; NOS2, nitric oxide synthase 2, inducible [*Mus musculus*]; OASL, 2'-5'-oligoadenylate synthetase like [*Homo sapiens*]; PAX3, paired box 3 [*Mus musculus*]; PDCD1LG2/PD-L2, programmed cell death 1 ligand 2 [*Homo sapiens*]; Pdcd1lg2/PD-L2, programmed cell death 1 ligand 2 [*Mus musculus*]; Pitx1, paired-like homeodomain transcription factor 1 [*Mus musculus*]; POU5F1/OCT3, POU class 5 homeobox 1 [*Homo sapiens*]; Pou5f1/Oct3/4, POU domain, class 5, transcription factor 1 [*Mus musculus*]; Ppia, peptidylprolyl isomerase A [*Mus musculus*]; PROM1/CD133, prominin 1 [*Mus musculus*; *Homo sapiens*]; Rcor2, REST corepressor 2 [*Mus musculus*]; REST, RE1-silencing transcription factor [*Mus musculus*]; RFX, regulatory factor X-associated protein [*Mus musculus*]; Ripk3, receptor-interacting serine-threonine kinase 3 [*Mus musculus*]; RUNX1, runt related transcription factor 1 [*Mus musculus*]; Serpin/Serpinb2, serine (or cysteine) peptidase inhibitor, clade B, member 2 [*Mus musculus*]; Slc6a6, solute carrier family 6 (neurotransmitter transporter, taurine), member 6 [*Mus musculus*]; Sna1, snail family zinc finger 1 [*Mus musculus*]; Sox2, SRY (sex determining region Y)-box 2 [*Mus musculus*]; SOX2, SRY-box transcription factor 2 [*Homo sapiens*]; Spire1, spire type actin nucleation factor 1 [*Mus musculus*]; STAT1, signal transducer and activator of transcription 1 [*Homo sapiens*]; Sting1, stimulator of interferon response cGAMP interactor 1 [*Mus musculus*]; Tap1, transporter 1, ATP-binding cassette, sub-family B (MDR/TAP) [*Mus musculus*]; Tap2, transporter 2, ATP-binding cassette, sub-family B (MDR/TAP) [*Mus musculus*]; Tbx4, T box 4 [*Mus musculus*]; TEAD, TEA domain family member 1 [*Mus musculus*]; Tfcp2, transcription factor CP2 [*Mus musculus*]; Ticam1/TRIF, toll-like receptor adaptor molecule 1 [*Mus musculus*]; Tlr3, toll-like receptor 3 [*Mus musculus*]; Tlr5, toll-like receptor 5 [*Mus musculus*]; Trpm4, transient receptor potential cation channel, subfamily M, member 4 [*Mus musculus*]; Ttll7, tubulin tyrosine ligase-like family, member 7 [*Mus musculus*]; Twist1, twist basic helix-loop-helix transcription factor 1 [*Mus musculus*]; Uba7, ubiquitin-like modifier activating enzyme [*Mus musculus*]; Vim, vimentin [*Mus musculus*]; Wee1, WEE 1 homolog 1 (S. pombe) [*Mus musculus*]; ZBTB, Zinc finger and BTB domain-containing protein [*Mus musculus*]; Zeb1, zinc finger E-box binding homeobox 1[*Mus musculus*].

Figures

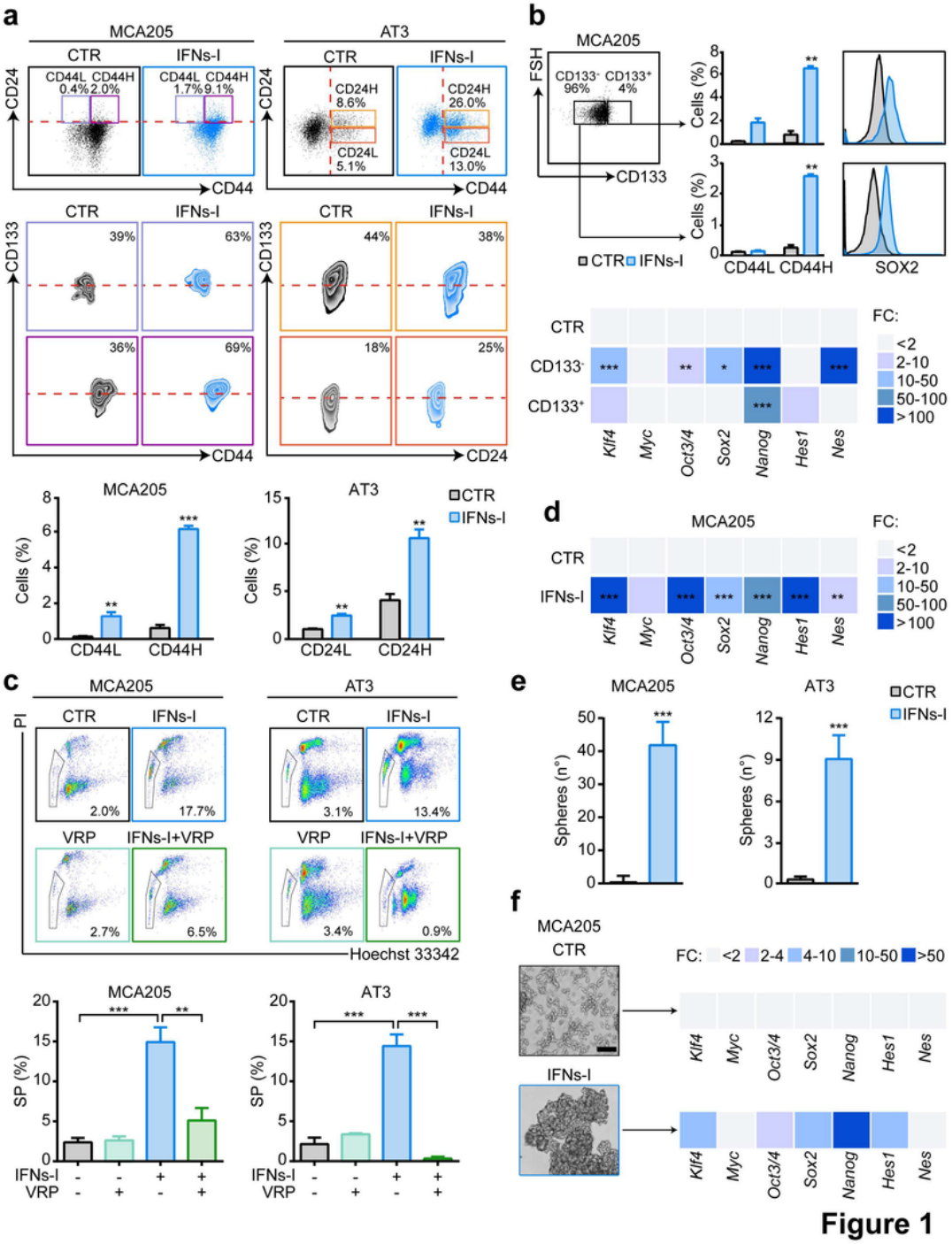

Figure 1

Figure 1

CSC appearance following IFN-I treatment. (a) Multiparametric flow cytometry analysis of the illustrated CSC surface markers in MCA205 and AT3 murine cell lines treated with mock (CTR) or purified IFNs-I (6000 U/mL, 72h). Representative biparametric plots and a histogram showing the percentage (mean±SEM; n≥3) of CD133+CD24+CD44+ cells obtained by calculating CD133+ cells within CD24+CD44+ subsets are shown. (b) Flow cytometry and qRT-PCR analyses of the reported CSC markers

and reprogramming factors in FACS-isolated CD133- and CD133+ MCA205 cells, mock- or IFN-I-treated. One representative experiment out of three is shown. qRT-PCR data are reported as mean FC over untreated condition after intrasample normalization to Ppia expression levels. (c) Flow cytometry analysis showing the proportion of SP (Hoechst 33342- within PI-) cells in MCA205 (n≥3) and AT3 (n=3) cells left untreated (black) or treated with VRP (100 μM, light green), IFNs-I (blue) or VRP+IFNs-I (dark green). Data are presented as mean±SEM. (d) qRT-PCR analysis of the expression levels of the illustrated reprogramming factors in MCA205 cells treated with IFNs-I (6000 U/mL, 72h). Data (n≥3) are reported as in b. (e) Clonogenic potential of MCA205 and AT3 cells mock- or IFN-I-treated and plated in soft-agar. The histograms represent the number of spheres (mean±SEM; n=10) generated, while representative images (f) show the capability of soft-agar-recovered IFN-I-treated MCA205 cells to grow as 3-D spheres in standard CSC culture conditions and to maintain a CSC-like transcriptomic profile. Scale bar=100 μm. *P<0.05, **P<0.01, ***P<0.001 (a,b,d,e) unpaired t test with Welch's correction, (c) ordinary one-way ANOVA test followed by Bonferroni's correction. See also Supplementary Figure 1. CD24H, CD133+CD44+CD24+high; CD24L, CD133+CD44+CD24+low; CD44H, CD133+CD24+CD44+high; CD44L, CD133+CD24+CD44+low; CSC, cancer stem cell; CTR, control; FC, fold change; IFNs-I, Type I interferons; PI, propidium iodide; SP, side population; VRP, verapamil.

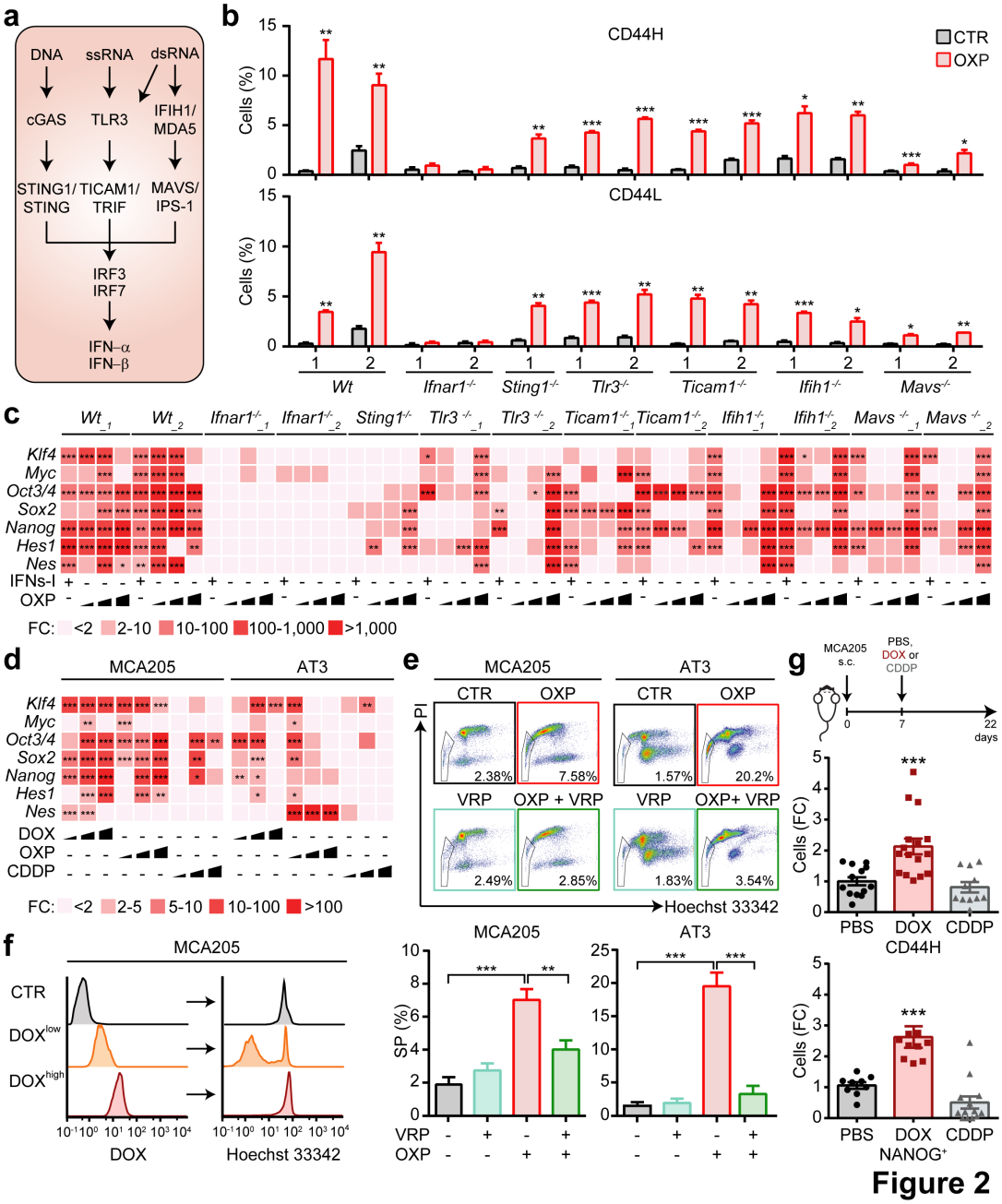

Figure 2

Figure 2

CSC promotion by immunogenic chemotherapy. (a) Major intracellular pathways upstream of IFNs-I. (b) Multiparametric flow cytometry analysis of CSC surface markers in MCA205-derived clones with the indicated genotypes left untreated (CTR) or treated with OXP (300 μM, 48h). The histograms represent the percentage (mean±SEM; n≥3) of CD44H and CD44L cells. (c,d) Quantification by qRT-PCR of the expression levels of the illustrated reprogramming factors in MCA205 clones left untreated or exposed to

OXP (3, 30, 300 μM, 48h) or IFNs-I (6000 U/mL) (c) and in MCA205 and AT3 cells left untreated or administered with DOX (0.25, 2.5, 25 μM), OXP (3, 30, 300 μM), or CDDP (1.5, 15, 150 μM) (d). Data are reported as mean FC over untreated condition (n≥2 in c and n≥3 in d) after intrasample normalization to the expression levels of Ppia. (e) Cytofluorometric evaluation of the proportion SP cells (Hoechst 33342-within PI- cells) upon treatment of MCA205 and AT3 cells with OXP in the presence or not of VRP (100 μM). Representative plots and quantitative analysis of the percentage of SP cells (mean±SEM; n≥3) are shown. (f) Flow cytometry analysis of DOX efflux ability in MCA205 cells left untreated (in grey) or exposed to DOX (2.5 μM, 48h). The two DOXlow (orange) and DOXhigh (red) DOX-treated cell subsets display high and low capability to efflux DOX and Hoechst 33342. (g) Ex vivo flow cytometric analysis of CSC surface markers and intracellular NANOG expression in MCA205 cells grown in C57BL/6J mice treated intratumorally with vehicle (PBS) or 2.9 mg/kg DOX or 2.5 mg/kg CDDP (n≥9 mice/group). Data are presented as mean FC±SEM over PBS treatment. *P<0.05, **P<0.01, ***P<0.001 (b,g) unpaired t test with Welch's correction and Mann-Whitney test, (c) ordinary two-way ANOVA test followed by Bonferroni's correction (d,e) ordinary one-way ANOVA test followed by Bonferroni's correction. See also Supplementary Figure 2. CD44H, CD133+CD24+CD44+high; CD44L, CD133+CD24+CD44+low; CDDP, cisplatin; CSC, cancer stem cell; CTR, control; DOX, doxorubicin; FC, fold change; IFNs-I, Type I interferons; OXP, oxaliplatin; PBS, phosphate buffered saline; PI, propidium iodide; SP, side population; VRP, verapamil.

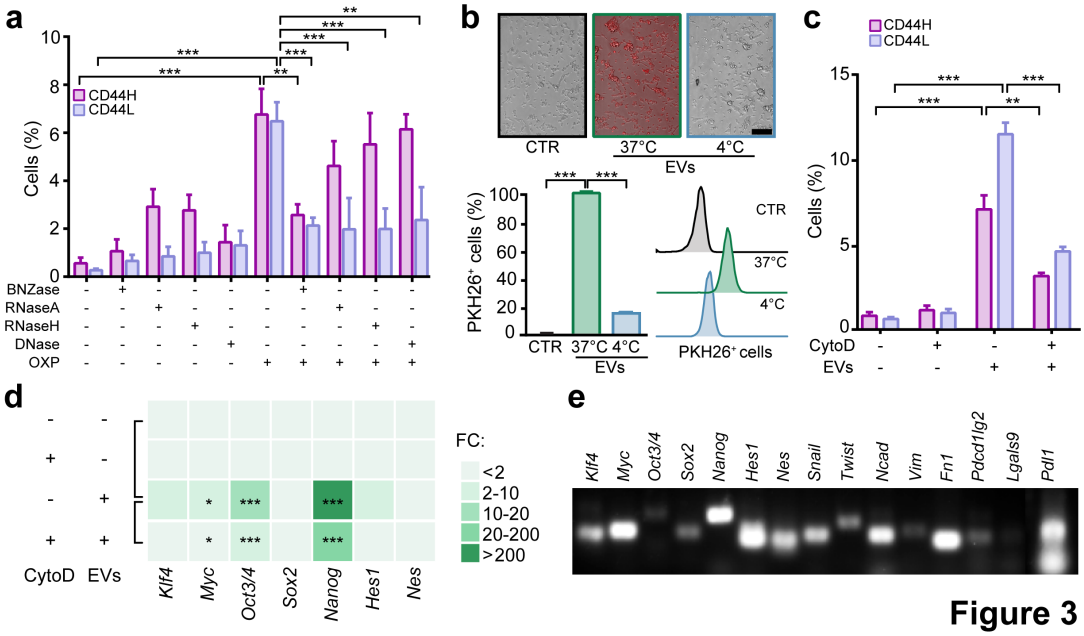

Figure 3

Figure 3

Cell-to-cell horizontal transfer of nucleic acids and de-differentiating factors during immunogenic chemotherapy. (a) Multiparametric flow cytometry analysis of CSC surface markers in “receiving” viable MCA205 cells upon co-culturing with “donor” MCA205 cells left untreated or previously treated with OXP (300 μM, 48h) alone or in combination with the indicated nucleases. Columns represent the percentage of CD44H and CD44L MCA205 cells, expressed as mean±SEM (n≥3). (b) Fluorescence microscopy (upper

panel) or flow cytometry (lower panel) analysis of the internalization (at 37°C and 4°C) of donor cell-derived, PKH26-stained EVs by “receiving” MCA205 cells. Scale bar: 100 μm. One representative experiment out of two is shown. (c) Multiparametric flow cytometry analysis of CSC surface markers in “receiving” MCA205 cells co-cultured with “donor” MCA205 cell-derived EVs in the presence of cyto D (0.5 μM). Data are presented as mean±SEM (n≥3). (d) Assessment of the expression levels of the indicated reprogramming factors by qRT-PCR in “receiving” MCA205 cells stimulated with “donor” MCA205 cell-derived EVs alone or in the presence of cyto D, as described in c. Data are reported as mean FC±SEM over control conditions of at least three independent experiments after intrasample normalization to Ppia expression levels. (e) Characterization of EV cargo by PCR analysis of a panel of the reported genes. *P<0.05, **P<0.01, ***P<0.001 (a-d) one-way ANOVA test followed by Bonferroni’s correction. See also Supplementary Figure 3. BNZase, benzonase; CD44H, CD133+CD24+CD44+high; CD44L, CD133+CD24+CD44+low; CSC, cancer stem cell; CTR, control; cyto D, cytochalasin D; EV, extracellular vesicles; FC, fold change; ICD, immunogenic cell death; OXP, oxaliplatin.

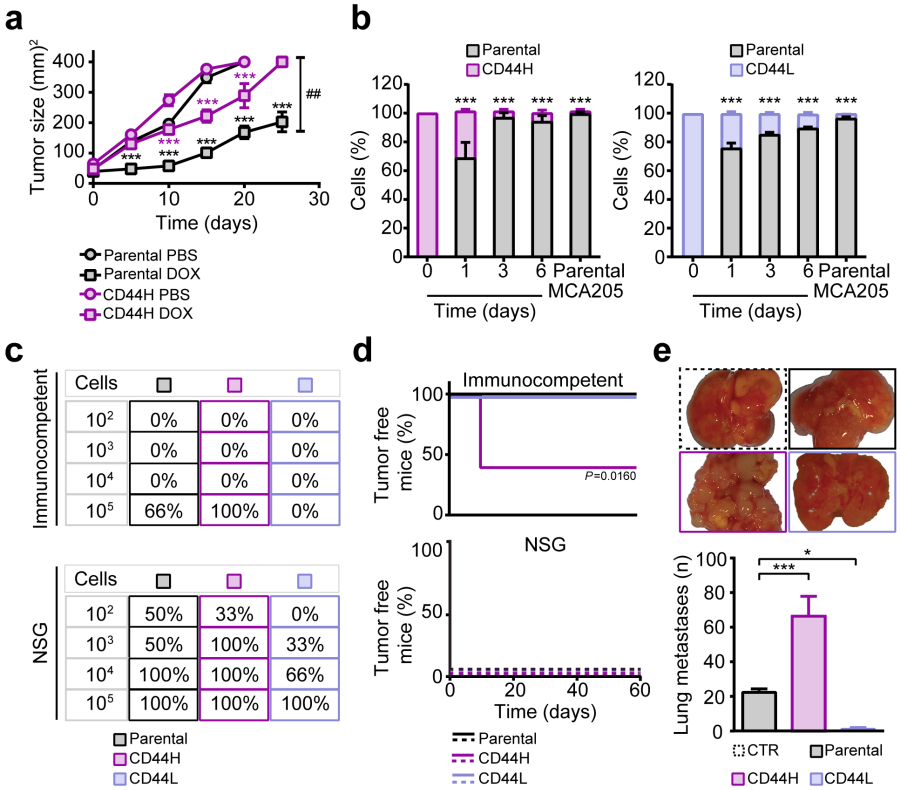

Figure 4

Figure 4

Functional characterization of ICD-CSCs. (a) Tumor growth of parental and CD44H MCA205 cells in C57BL/6J mice (n=6 mice/group), treated either with PBS or DOX (2.9 mg/kg). Growth curves show the mean tumor surface±SEM in one representative experiment out of two. (b) Flow cytometry analysis of the regenerative potential of FACS-isolated CD44H and CD44L MCA205 cells upon OXP treatment followed by cultivation in standard conditions for the indicated time. The histograms report the change in the

percentage of ICD-CSCs evaluated by flow cytometry. (c,d) In vivo evaluation of the tumorigenic (c) and prophylactic (d) potential of parental MCA205 and ICD-CSCs upon inoculation in immunocompetent C57Bl/6J or immunodeficient NSG mice at the indicated dose (n=3 mice/group). In d, 1x105 parental MCA205 cells were injected in the other flank of immunocompetent or immunodeficient mice of c that rejected the first injection. The percentage of tumor-free mice was the endpoint analyzed. (e) In vivo evaluation of the metastatic potential of parental MCA205 or ICD-CSCs injected via the tail vein of immunocompetent C57Bl/6J mice (n=3 mice/group). Representative macroscopic observation of lung metastases 15 days post injection and quantification of the number of lung metastases in one representative experiment out of two are reported. *P<0.05, **P<0.01, ***P<0.001 (a,b) two-way RM ANOVA (a) and ordinary two-way ANOVA (b) tests followed by Bonferroni's correction and unpaired t test with Welch's correction (d) Log-rank Mantel-Cox test (e) one-way ANOVA test followed by Bonferroni's correction. See also Supplementary Figure 4. CD44H, CD133+CD24+CD44+high; CD44L, CD133+CD24+CD44+low; CSC, cancer stem cell; DOX, doxorubicin; IFNs-I, Type I IFNs; MTX, mitoxantrone; NSG, NOD SCID gamma; OXP, oxaliplatin; PBS, phosphate buffered saline.

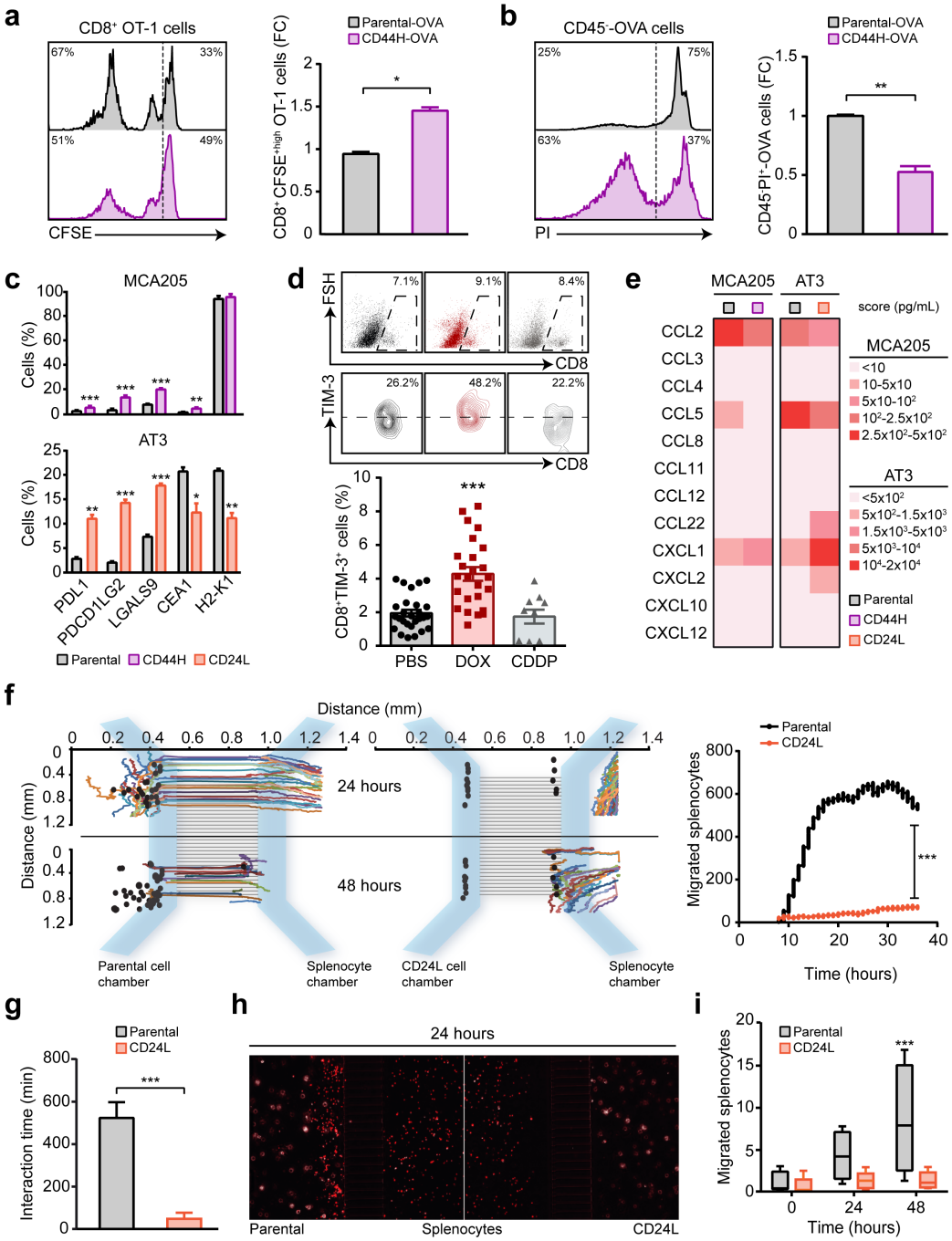

Figure 5

Figure 5

Phenotypic and functional profiling of IFN-CSC immunogenicity. (a) Flow cytometry analysis of the proliferation rate of CFSE-stained CD8+ OT-1 T cells stimulated with OVA-expressing parental or CD44H cells. The histograms represent the FC (mean±SEM; n=3) of not-proliferating CFSE+highCD8+ cells. (b) Flow cytometry analysis of the ability of CD45- OVA-expressing parental and CD44H cells to resist CD8+ OT-1-mediated killing. The histograms represent the FC (mean±SEM; n=3) of dying PI+CD45- cells. (c)

Multiparametric flow cytometry analysis of the indicated IC molecules in MCA205 or AT3 cells (parental and ICD-CSCs). Data are presented as mean±SEM with n≥3. (d) Flow cytometry analysis of TIM-3 expression in CD8+ TILs from MCA205-derived xenografts 15 days post in vivo intratumoral treatment with PBS, or DOX (2.9 mg/kg), or CDDP (2.5 mg/kg) (n≥10 mice/group). Data are presented as mean±SEM of three independent experiments. (e) Quantification of released chemokines in supernatants from MCA205 and AT3 cells (parental and ICD-CSCs) by Luminex Multiplex Assay. One representative experiment out of two is shown. (f-i) Time-lapse analysis of the migration of H-2Kb splenocytes towards parental and CD24L AT3 cells in microfluidic devices. Plots representing the trajectories of individual splenocytes towards target cancer cells (black spots) recorded in time-lapse are reported in f (n=820), while quantification of the interaction times between splenocytes and parental or CD24L ICD-CSCs are shown in g (n≥10 cells per condition analyzed; see also Supplementary Movies 1-4). Representative pictures of splenocytes in competition microfluidic devices (scale bar: 100 μm) and quantification of splenocytes migrated towards parental or CD24L ICD-CSCs are shown in h and i, respectively. Data are expressed as mean±SEM (n≥4). *P<0.05, **P<0.01, ***P<0.001 (a-c,f) unpaired t test with Welch's correction and one-way ANOVA test followed by Bonferroni's correction, (d,g) Mann-Whitney test, (i) two-way RM ANOVA test followed by Bonferroni's correction. See also Supplementary Figure 4 and Supplementary Movies 1-4. CD24L, CD133+CD44+CD24+low; CD44H, CD133+CD24+CD44+high; CDDP, cisplatin; CFSE, carboxyfluorescein succinimidyl ester; CSC, cancer stem cell; DOX, doxorubicin; FC, fold change; ICs, immune checkpoints; ICD-CSCs, immunogenic cell death-induced cancer stem cells; OVA, ovalbumin; PBS, phosphate buffered saline; TILs, tumor infiltrating lymphocytes.

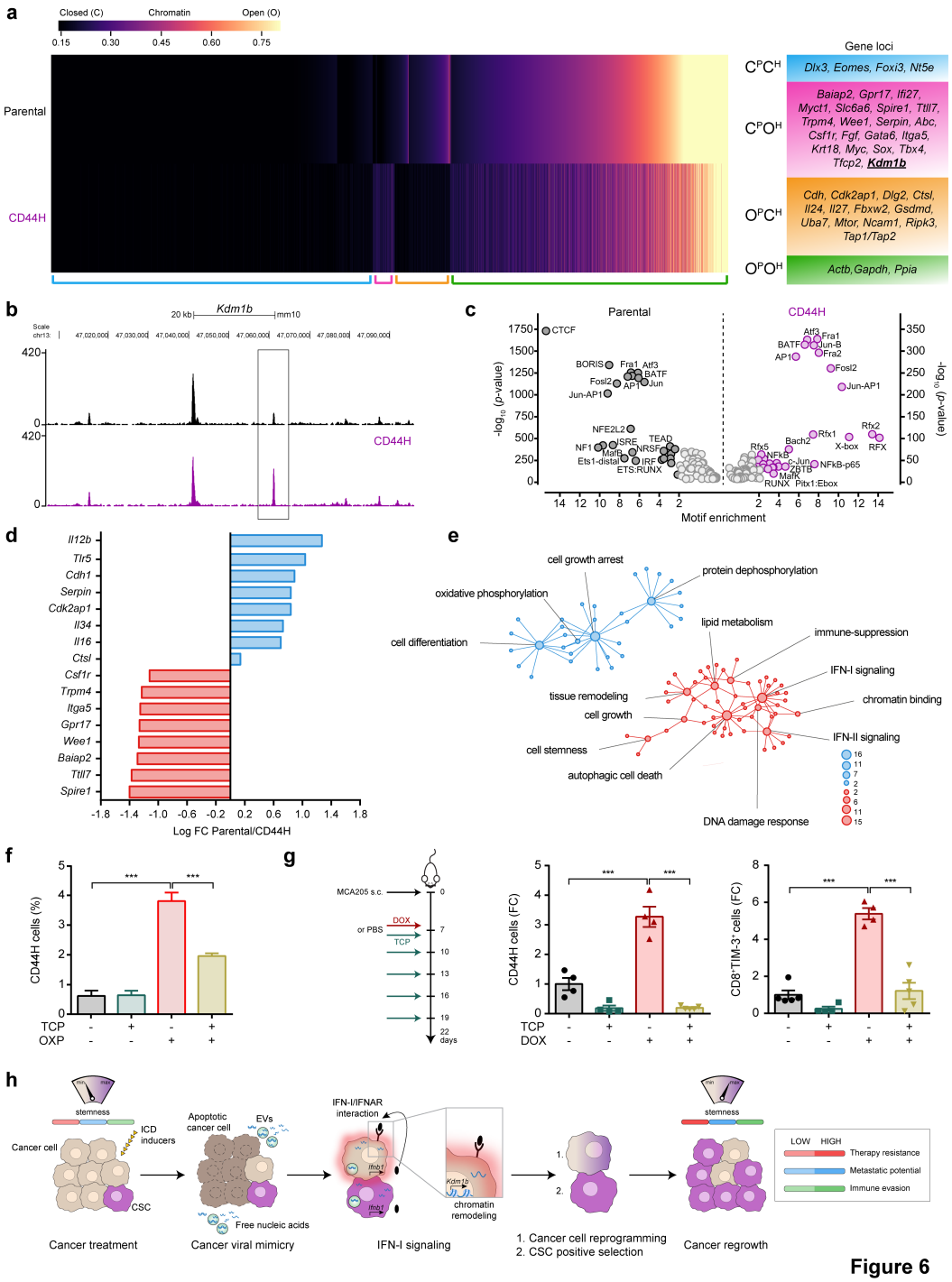

Figure 6

Figure 6

IFN-I-driven chromatin remodeling. (a-e) ATAC-seq (a-c) and RNA-seq (d,e) analysis in parental or FACS-isolated CD44H MCA205 cells upon enrichment via IFN-I administration (6000 U/mL, 72h). The heatmap in a illustrates global open (O) or closed (C) status of genes in parental (P) and CD44H (H) cells and gene stratification in 4 subgroups according to chromatin accessibility profiles: C or O in all samples (CPCH) and (OPOH), and differentially O or C in the two cell subsets (CPOH and OPCH). Representative genes for

each subgroup are shown. In b, representative loci for Kdm1b within CPOH group are illustrated. (c) TF family binding motifs enriched at least 2-fold in loci more accessible in parental (black) or CD44H (purple) cells; the x axis shows the log FC of TF motif enrichment in target cells (either parental or CD44H) over non-target cells; the y axis depicts the significance level of enrichment. (d) Patterns of gene expression as determined by RNA-seq for representative ATAC-seq-identified genes. (e) Genes upregulated (red) and downregulated (blue) in CD44H IFN-CSCs were used to generate a GO network analysis, visualized by using clusterProfiler and enrichPlot R packages. Nodes represent enriched GO-terms, whereas node size represents the corresponding FDR-adjusted enrichment P value (q value). (f) Multiparametric flow cytometry analysis showing the percentage of CD44H ICD-CSCs upon OXP (300 μM, 48h) treatment alone or in combination with the KDM1B inhibitor TCP (10 μM). Data are presented as mean±SEM (n≥4). (g) Schematic experimental protocol of in vivo KDM1B inhibition (left panel) and multiparametric flow cytometry analysis showing the FC of CD44H (central panel) and CD8+TIM-3+ (right panel) cells in tumoral bulks from C57Bl/6J mice treated with DOX (2.9 mg/Kg) in combination or not with TCP (5 mg/Kg) (n≥4 mice/group). (h) Graphical summary. ***P<0.001 (ordinary one-way ANOVA test followed by Bonferroni's correction). See also Supplementary Figure 5. CD44H, CD133+CD24+CD44+high; FC, fold change; FDR, false discovery rate; GO, gene ontology; ICD-CSCs, immunogenic cell death-induced cancer stem cells; IFNs-I, Type I IFNs; TCP, tranylcypromine; TF, transcriptional factor.

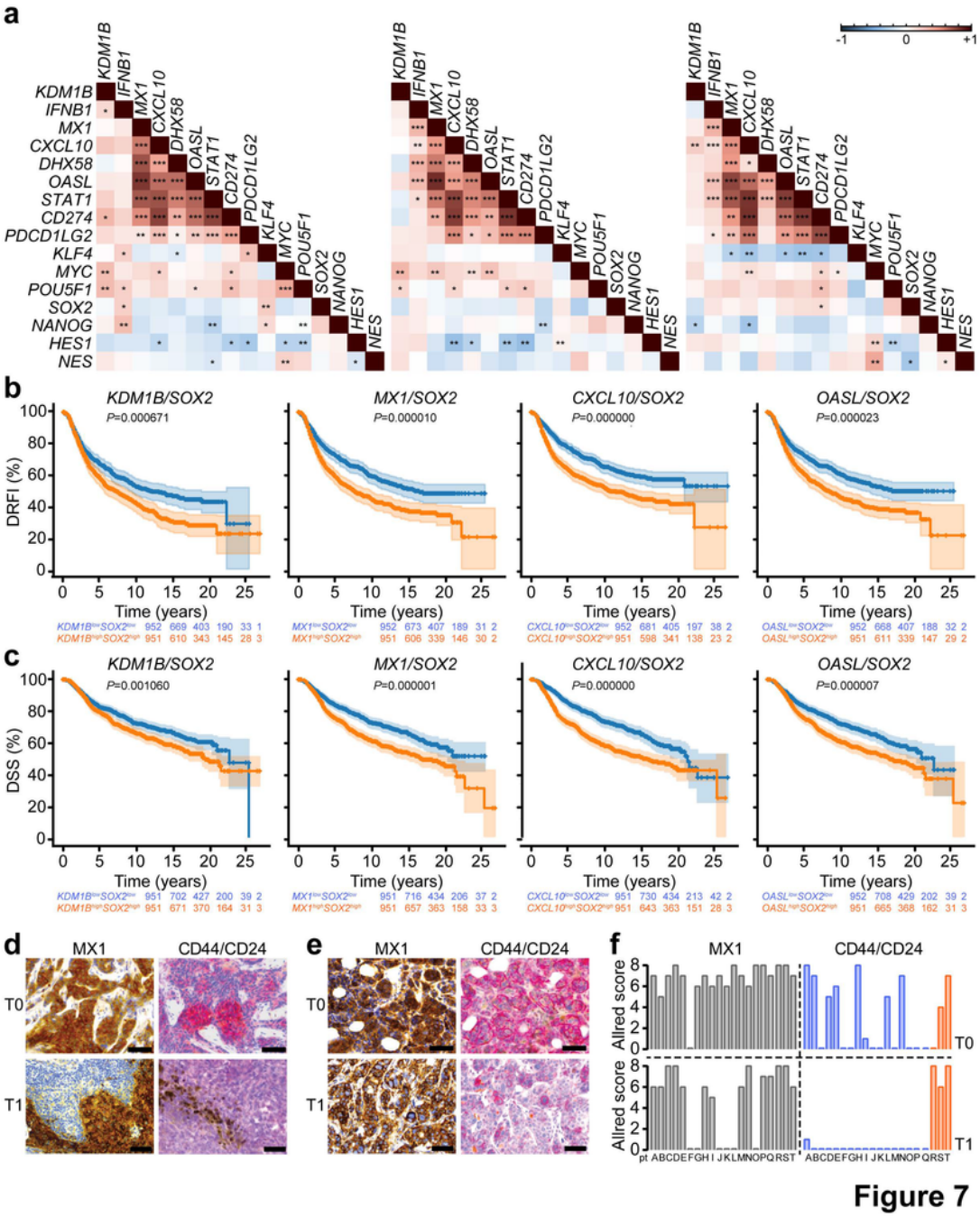

Figure 7

Figure 7

Correlation between KDM1B, IFN-I signature, stemness and immune evasion in BC patients. (a) Spearman correlations between KDM1B, IFN-I-related, CSC-related and IC-related gene expression scores from microarray data of three publicly available cohorts of BC patients treated with neo-adjuvant anthracycline-based chemotherapy. *P<0.05, **P<0.01, ***P<0.001. (b,c) Kaplan-Meier plots depicting DRFI (b) and DSS (c) in BC patients stratified according to risk behaviour via the Metabric platform

(https://ega-archive.org/) and expressing low (blue curves) or high (orange curves) levels of SOX2 (GenBank/Entrez ID: 6657) and either KDM1B (GenBank/Entrez ID: 221656), or MX1 (GenBank/Entrez ID: 4599), or CXCL10 (GenBank/Entrez ID: 3627), or OASL (GenBank/Entrez ID: 8638). P Cox, Log-Rank (Mentel-Cox) P value was calculated using the Metabric website. P values 0.05 were considered statistically significant. (d-f) IHC analysis of 20 paraffin-embedded paired BC biopsies at T0 (diagnosis) and T1 (surgery) using antibodies directed against MX1, CD45 and CD44+CD24. Representative IHC images from sections of two patients are reported in d and e (scale bar=30 μm), while Allred MX1 and CD44+CD24+low/- scores for 20 patients at T0 and T1 are shown in f. In f, orange hystograms represent patients showing an increase of CSCs after therapy. See also Supplementary Figure 6. BC, breast carcinoma; CSCs, cancer stem cells; DRFI, distant relapse free incidence; DSS, disease specific survival; ICs, immune checkpoints; IFNs-I, Type I IFNs; IHC, immunohistochemistry.

Supplementary Files

This is a list of supplementary files associated with this preprint. Click to download.

- SupplementaryMovie1MusellaetalNI.avi
- SupplementaryMovie2MusellaetalNI.avi
- SupplementaryMovie3MusellaetalNI.avi
- SupplementaryMovie4MusellaetalNI.avi
- SupplementaryInformationMusellaetal2021.pdf